

1 **Two-dimensional hybrid particle-in-cell simulations of**  
2 **magnetosonic waves in the dipole magnetic field: On a**  
3 **constant  $L$ -shell**

4 **Kyungguk Min<sup>1</sup>, Kaijun Liu<sup>2</sup>, Richard E. Denton<sup>3</sup>, František Němec<sup>4</sup>, Scott**  
5 **A. Boardsen<sup>5,6</sup>, Yoshizumi Miyoshi<sup>7</sup>**

6 <sup>1</sup>Department of Astronomy and Space Science, Chungnam National University, Daejeon, Korea.

7 <sup>2</sup>Department of Earth and Space Sciences, Southern University of Science and Technology, Shenzhen,  
8 China.

9 <sup>3</sup>Department of Physics and Astronomy, Dartmouth College, Hanover, New Hampshire, USA.

10 <sup>4</sup>Faculty of Mathematics and Physics, Charles University, Prague, Czech Republic.

11 <sup>5</sup>NASA/GSFC, Greenbelt, Maryland, USA.

12 <sup>6</sup>Goddard Planetary Heliophysics Institute, University of Maryland, Baltimore County, Maryland, USA.

13 <sup>7</sup>ISEE, Nagoya University, Nagoya, Japan.

14 **Key Points:**

- 15 • 2D hybrid PIC simulations are carried out on a constant  $L$ -shell surface to sim-  
16 ulate the excitation of MSWs for the first time  
17 • Despite the extended unstable region in latitude, MSWs do not grow well if they  
18 get latitudinally out of resonance  
19 • Scattering of ring-like protons during MSW excitation is local so that those pro-  
20 tons do not necessarily follow Liouville's theorem

## Abstract

Two-dimensional hybrid particle-in-cell (PIC) simulations are carried out on a constant  $L$ -shell (or drift shell) surface of the dipole magnetic field to investigate the generation process of near-equatorial fast magnetosonic waves (a.k.a equatorial noise; MSWs hereafter) in the inner magnetosphere. The simulation domain on a constant  $L$ -shell surface adopted here allows wave propagation and growth in the azimuthal direction (as well as along the field line) and is motivated by the observations that MSWs propagate preferentially in the azimuthal direction in the source region. Furthermore, the equatorial ring-like proton distribution used to drive MSWs in the present study is (realistically) weakly anisotropic. Consequently, the ring-like velocity distribution projected along the field line by Liouville's theorem extends to rather high latitude, and linear instability analysis using the local plasma conditions predicts substantial MSW growth up to  $\pm 27^\circ$  latitude. In the simulations, however, the MSW intensity maximizes near the equator and decreases quasi-exponentially with latitude. Further analysis reveals that the stronger equatorward refraction at higher latitude due to the larger gradient of the dipole magnetic field strength prevents off-equatorial MSWs from growing continuously, whereas MSWs of equatorial origin experience little refraction and can fully grow. Furthermore, the simulated MSWs exhibit a rather complex wave field structure varying with latitude, and the scattering of energetic ring-like protons in response to MSW excitation occurs faster than the bounce period of those protons so that they do not necessarily follow Liouville's theorem during MSW excitation.

## 1 Introduction

Near-equatorial fast magnetosonic waves (MSWs hereinafter) are among the most frequently observed plasma waves in the inner magnetosphere (radial distances  $\lesssim 10 R_E$ , where  $R_E$  is Earth radius) and have the largest amplitude in the frequency band between a few Hz and  $\sim 100$  Hz (Santolík et al., 2004; Meredith et al., 2008; Ma et al., 2013; Hrbáčková et al., 2015; Posch et al., 2015; Boardsen et al., 2016). MSWs are also referred to as equatorial noise after the initial discovery by Russell et al. (1970). Soon after, it was found that the noise-like emissions near the equator can be described as the oblique whistler mode or the high-frequency extension of the fast magnetosonic mode in a proton-electron plasma (Boardsen et al., 1992; Němec et al., 2006; Walker et al., 2015; Boardsen et al., 2016). The defining characteristic of MSWs includes a series of spectral peaks at or near harmonics of the proton cyclotron frequency,  $f_{cp}$ , between  $f_{cp}$  and the lower hybrid frequency; high magnetic compressibility,  $|\delta B_{\parallel}|^2 \gg |\delta B_{\perp}|^2$  (e.g., Perraut et al., 1982; Boardsen et al., 1992; Santolík et al., 2004; Boardsen et al., 2016); and propagation quasi-perpendicular to the background magnetic field. (Throughout the paper, subscripts  $\parallel$  and  $\perp$  indicate the directions parallel and perpendicular to the background magnetic field, respectively.) Also, according to the cold plasma magnetosonic mode dispersion relation, the longitudinal component of the wave electric field is much greater than the transverse component for frequencies greater than about  $3f_{cp}$  (see, e.g., Boardsen et al., 2016, Figure 1); this has been used to observationally determine the equatorial propagation direction of MSWs (Santolík et al., 2002; Němec et al., 2013; Boardsen et al., 2018). The generation of MSWs most likely involves proton cyclotron resonant interactions with energetic protons having a ring-like velocity distribution with a positive slope in the perpendicular velocity direction,  $\partial f / \partial v_{\perp} > 0$  (Gulelmi et al., 1975; Gurnett, 1976; Perraut et al., 1982; Boardsen et al., 1992; Horne et al., 2000; Chen et al., 2010; Liu et al., 2011).

Observations (Gurnett, 1976; Perraut et al., 1982; Laakso et al., 1990; Kasahara et al., 1994; André et al., 2002; Santolík et al., 2004; Němec et al., 2005; Němec et al., 2006; Němec et al., 2015; Hrbáčková et al., 2015; Boardsen et al., 2016; Yuan et al., 2019; Zou et al., 2019) have shown that MSWs occur most frequently within  $10^\circ$  latitude from the magnetic equator and their amplitudes likewise exhibit a narrow latitudinal extent with a peak at the magnetic equator. It was also shown that the propagating MSWs are

73 mode-converted to plasmaspheric EMIC waves in the lower  $L$ -shells (Horne & Miyoshi,  
 74 2016; Miyoshi et al., 2019). Based on ray tracing analyses, it has long been suggested  
 75 that wave sources are similarly located near the magnetic equator (e.g., Boardsen et al.,  
 76 1992; Horne et al., 2000; Shklyar & Balikhin, 2017). MSWs generated from an equato-  
 77 rial source region with a wave normal angle,  $\theta_{\mathbf{k}}$ , deviating from  $90^\circ$  can propagate away  
 78 from the source region toward higher latitudes. As they propagate, their  $\theta_{\mathbf{k}}$  approaches  
 79  $90^\circ$  due to refraction, and the waves are eventually reflected back toward equator (Boardsen  
 80 et al., 1992, Figures 5 and 8). Due to the quasi-perpendicular propagation, most of the  
 81 MSWs generated at an equatorial source region will remain close to the magnetic equa-  
 82 tor. Furthermore, the MSWs that are reflected at high latitude experience a shorter du-  
 83 ration of wave growth (or a longer duration of damping) than the waves that remain at  
 84 the equator, hence explaining the observed amplitude peak at the equator. This is be-  
 85 cause the largest wave growth occurs close to harmonics of the local  $f_{\text{CP}}$  and close to  $\theta_{\mathbf{k}} =$   
 86  $90^\circ$  (e.g., Boardsen et al., 1992; Chen, 2015). Boardsen et al. (1992, 2016) argued that  
 87 the harmonic-dependent reflection latitude can account for the frequently observed, funnel-  
 88 shaped features in frequency-time spectrograms: For similar equatorial  $\theta_{\mathbf{k}}$ , lower-frequency  
 89 MSWs are more closely confined to the magnetic equator than higher-frequency MSWs;  
 90 and for similar reflection latitude, lower-frequency MSWs experience stronger damping  
 91 while passing through the same equatorial region (Boardsen et al., 1992, Figure 9); how-  
 92 ever, a follow-up study using gain analysis was not performed. Zhima et al. (2015) an-  
 93 alyzed MSWs that were observed at about  $-17^\circ$  latitude and which exhibited discrete  
 94 spectral peaks with frequency spacing of adjacent spectral lines not equal to the local  
 95  $f_{\text{CP}}$ . Using backward ray tracing, they suggested that propagation from spatially nar-  
 96 row equatorial source regions can account for the observed discrete spectral structures.

97 In recent years, much attention has been paid to the spatial distribution of MSWs  
 98 and their dispersion properties (e.g., Zou et al., 2019; Ma et al., 2019) because of the po-  
 99 tential role that they play in accelerating and scattering radiation belt electrons. It has  
 100 been demonstrated that radiation belt electrons can interact with MSWs through Lan-  
 101 dau resonance (Horne et al., 2007), transit-time scattering (Bortnik & Thorne, 2010),  
 102 and bounce resonance (Chen et al., 2015; Li et al., 2015). Horne et al. (2007) was the  
 103 first to suggest that electron acceleration can occur via Landau resonance with scatter-  
 104 ing rates comparable to those for whistler mode chorus. Bortnik and Thorne (2010) demon-  
 105 strated that the lack of parallel wave field structure (due to quasi-perpendicular prop-  
 106 agation) and the equatorial confinement of MSWs can cause a new type of scattering ef-  
 107 fect called the transit-time effect. They suggested that Landau resonance with electrons  
 108 is only effective near the equator where average  $\theta_{\mathbf{k}}$  of MSWs becomes minimum (accord-  
 109 ing to the equator-wave-source mechanism), whereas transit-time scattering is able to  
 110 scatter electrons over the entire latitudinal extent of the waves. On the other hand, bounce  
 111 resonance with MSWs can be particularly important for the scattering of near-equatorially-  
 112 mirroring electrons (Roberts & Schulz, 1968; Shprits, 2009). Considering that MSWs are  
 113 generated near the equator and propagate away from it, Tao and Li (2016) and Li and  
 114 Tao (2018) showed that the bounce resonance is sensitive to the  $\theta_{\mathbf{k}}$  distribution and the  
 115 latitudinal extent of wave power. Furthermore, the bounce diffusion rate can be com-  
 116 parable to the diffusion rate caused by Landau resonance.

117 Self-consistent particle-in-cell (PIC) simulations of plasma waves in the inner mag-  
 118 netosphere are useful not only to understand the generation process of waves but to quan-  
 119 tify their effect on energetic electrons in the Van Allen belts. Moreover, they can com-  
 120 plement the limitations of observations that have to contend with the limited spatiotem-  
 121 poral coverage, measurement quality, and limited high-resolution datasets. Unlike elec-  
 122 tromagnetic ion cyclotron (EMIC) waves and whistler-mode chorus (e.g., Denton et al.,  
 123 2014; Denton, 2018; Lu et al., 2019), however, self-consistent simulations of MSWs have  
 124 until recently been limited to homogeneous plasmas in a uniform background magnetic  
 125 field. Chen et al. (2018) carried out two-dimensional simulations of MSWs in a merid-  
 126 ional plane of a scaled-down dipole magnetic field for the first time, and were able to test

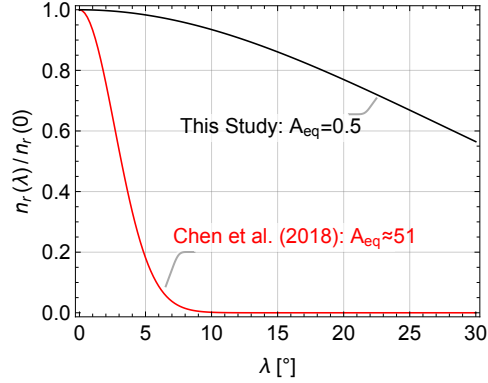


**Figure 1.** Comparison between the energetic proton ring density used in Chen et al. (2018) (red) and the partial shell density in this study (black), plotted versus latitude. Equivalent equatorial temperature anisotropies ( $A_{\text{eq}}$ ) are 51 and 0.5, respectively.

127 the equator-wave-source mechanism mentioned above. In their model, the free energy  
 128 source (i.e., energetic ring protons) was limited to well within  $\pm 10^\circ$  latitude (see Fig-  
 129 ure 1; red curve) and also in  $L$ -shell. According to their results, MSWs excited in that  
 130 equatorial source region were confined to the equator. Interestingly, the waves in their  
 131 simulation propagated in the radial direction with wave normal directions nearly per-  
 132 pendicular to the background magnetic field. They noted that the lack of wave struc-  
 133 ture along the field line indicates the importance of the transit-time effect over Landau  
 134 resonance. On the other hand, Min, Boardsen, et al. (2018) and Min et al. (2019) car-  
 135 ried out two-dimensional PIC simulations of MSWs on the equatorial plane of the dipole  
 136 magnetic field, focusing on the equatorial evolution with and without the steep density  
 137 gradient of the plasmopause.

138 The present study investigates the generation process of MSWs using two-dimensional  
 139 PIC simulations. We use the hybrid approach where the cool background electron and  
 140 proton populations are represented as cold fluids in simulations (e.g., Katoh & Omura,  
 141 2004; Tao, 2014). The major difference (other than the hybrid approach of the present  
 142 simulations) from Chen et al. (2018) is that the simulation domain is contained in a con-  
 143 stant  $L$ -shell surface instead of the meridional plane. This is to take into account the ob-  
 144 servational fact that the dominant MSW propagation is along the azimuthal direction  
 145 in the source region (Němec et al., 2013; Boardsen et al., 2018). Section 2 outlines the  
 146 motivation and goal of the present simulation study. Section 3 describes the simulation  
 147 setup, and section 4 presents the simulation results. Section 5 further discusses the sim-  
 148 ulation results and section 6 concludes the paper. To keep the paper brief, non-essential  
 149 materials including some considerations for the modeling approach are presented through  
 150 supporting information.

## 151 2 Motivation and Goal

152 Although Chen et al. (2018)’s simulations demonstrated the MSW excitation and  
 153 propagation consistent with the equator-wave-source mechanism, we find that some as-  
 154 sumptions in their model and some of their simulation results do not have strong obser-  
 155 vational support.

156 First, in order to limit the free energy source into a narrow latitudinal region, Chen  
 157 et al. (2018) had to use an equatorial temperature anisotropy of the proton ring distri-  
 158 bution equivalent to  $A_{\text{eq}} \equiv T_{\perp,\text{eq}}/T_{\parallel,\text{eq}} - 1 \approx 51$  (where  $T_{\parallel}$  and  $T_{\perp}$  are the effective

159 temperatures parallel and perpendicular to the background magnetic field, respectively,  
 160 and the subscript “eq” denotes that the quantities involved are the equatorial values).  
 161 According to Liouville’s theorem, the number density of a plasma population having a  
 162 pancake distribution at the equator decreases with increasing latitude (via dependence  
 163 on the magnetic field strength), and the more anisotropic the pancake distribution is,  
 164 the faster the ring/shell density decreases with latitude (e.g., Roederer, 1970). Figure  
 165 1 shows in red the number density as a function of latitude for the proton ring distri-  
 166 bution used in Chen et al. (2018). Although not impossible, such a large value of equa-  
 167 torial anisotropy is improbable for typical inner magnetospheric conditions (e.g., Thom-  
 168 sen et al., 2017). In addition, temperature anisotropy of that magnitude can lead to the  
 169 excitation of strong EMIC waves (e.g., Min et al., 2016), although their simulations do  
 170 not appear to show parallel-propagating EMIC waves within the time period of their sim-  
 171 ulation run. Apparently, one would want to test the generation process using the con-  
 172 ditions more commonly found in the inner magnetosphere. In fact, we use a value of equa-  
 173 torial temperature anisotropy,  $A_{\text{eq}} = 0.5$  based on the event analysis of Min, Liu, Wang,  
 174 et al. (2018), which lies at the bottom end of the anisotropy range surveyed by Thomsen  
 175 et al. (2017). As shown in Figure 1, the decrease of the energetic proton ring density is  
 176 much more gradual with this more realistic anisotropy value and there still exist a sub-  
 177 stantial fraction (60%) of energetic ring protons at  $30^\circ$  latitude. According to the com-  
 178 plementing linear analysis and kinetic simulations of Min and Liu (2020) using the lo-  
 179 cal plasma conditions along the field line, the saturation amplitudes of excited MSWs  
 180 monotonically decrease with latitude, although the initial growth rate maximizes away  
 181 from the equator (at around  $20^\circ$  latitude). This suggests that we may still achieve the  
 182 observed latitudinal wave confinement even with a wide latitudinal extent of the free en-  
 183 ergy source. (That is, a limited wave source region may not be necessary to produce lat-  
 184 itudinally limited MSWs.)

185 Second, recent observational studies (Němec et al., 2013; Boardsen et al., 2018) showed  
 186 that propagation of MSWs in low density regions (where the conditions are favorable for  
 187 wave excitation) is dominantly in the azimuthal direction. By simple ray tracing calcu-  
 188 lation assuming an azimuthally symmetric medium, Boardsen et al. (2018) predicted that  
 189 optimal wave growth at the source region will occur for waves propagating along the con-  
 190 tour of constant magnetic field magnitude (that is, in the azimuthal direction) rather than  
 191 in the radial direction. This was confirmed by Min, Boardsen, et al. (2018) from two-  
 192 dimensional PIC simulations of MSWs considering propagation exactly perpendicular  
 193 to the background magnetic field in the equatorial plane. So, for MSW simulations it  
 194 seems necessary to allow wave propagation in the azimuthal direction in order to prop-  
 195 erly model the generation process of MSWs in the source region. In the present study,  
 196 we choose a two-dimensional simulation domain on a constant  $L$ -shell surface in the dipole  
 197 magnetic field, which ignores the radial dependence of quantities. This is appropriate  
 198 because in the dipole magnetic field, all particles with the same drift invariant (or  $L^*$ )  
 199 share the same  $L$ -shell. On the other hand, the present setup suppresses radial propa-  
 200 gation of MSWs (and in fact any fluctuations), even though MSWs are known to nat-  
 201 urally refract radially outward (and inwards just inside the plasmopause) (Gulemi et  
 202 al., 1975; Chen & Thorne, 2012). Therefore, the present setup is not capable of simu-  
 203 lating the refraction of MSWs in the radial direction followed by their migration across  
 204 multiple  $L$ -shells, which has been shown both theoretically (e.g., Horne et al., 2000; Chen  
 205 & Thorne, 2012; Shklyar & Balikhin, 2017) and observationally (e.g., Němec et al., 2013;  
 206 Santolík et al., 2016). Consequently, we limit the scope of the present study to under-  
 207 standing the generation process of MSWs in the source region in a dipole magnetic field.

208 The last point concerns the lack of parallel wave structure in the simulation results  
 209 of Chen et al. (2018): MSWs excited in their simulations exhibited nearly field-aligned  
 210 wave fronts at all latitudes. This seems counterintuitive, because the ray tracing anal-  
 211 yses (e.g., Boardsen et al., 1992; Horne et al., 2000) show a varying wave normal angle  
 212 as a wave packet propagates along and across the field line. In addition, recent statis-

213 tical analysis by Zou et al. (2019) seems to indicate the change in the wave normal angle  
 214 with latitude such that the average  $\theta_{\mathbf{k}}$  is relatively narrowly peaked about  $90^\circ$  near  
 215 the equator and decreases monotonically with latitude, although we should note that they  
 216 presented no concrete analysis to show and understand the impact of the error in indi-  
 217 vidual  $\theta_{\mathbf{k}}$  measurements (see section 5). The discrepancy, or lack thereof, further mo-  
 218 tivates us to explore more realistic assumptions.

### 219 3 Simulation Setup

#### 220 3.1 Key Plasma Parameters

221 The initial simulation parameters used in the present study are based on those of  
 222 our earlier simulations (Min, Liu, Denton, & Boardsen, 2018; Min, Boardsen, et al., 2018),  
 223 which were derived from the actual MSW event studied in detail by Min, Liu, Wang, et  
 224 al. (2018) and Boardsen et al. (2018). The key observational parameters for the event  
 225 are: The equatorial radial distance is  $\sim 5.6 R_E$ , the equatorial (total) plasma number den-  
 226 sity is  $n_{e,\text{eq}} \approx 24 \text{ cm}^{-3}$ , and the equatorial magnetic field strength is  $B_{\text{eq}} \approx 131 \text{ nT}$ .  
 227 The corresponding electron plasma-to-cyclotron frequency ratio is  $\omega_{pe,\text{eq}}/\Omega_{ce,\text{eq}} \approx 12$ ,  
 228 and the light-to-Alfvén speed ratio is  $c/v_{A,\text{eq}} \approx 514$ , where  $\omega_{pe,\text{eq}} = \sqrt{4\pi n_{e,\text{eq}} e^2/m_e}$ ;  
 229  $\Omega_{ce,\text{eq}} = eB_{\text{eq}}/(m_e c)$ ; and  $v_{A,\text{eq}} = B_{\text{eq}}/\sqrt{4\pi m_p n_{e,\text{eq}}}$ . The Alfvén energy is  $E_{A,\text{eq}} \equiv$   
 230  $m_p v_{A,\text{eq}}^2/2 \approx 1.78 \text{ keV}$ . The subscript “eq” indicates that the quantity under consid-  
 231 eration is an equatorial value.

232 Since we desire to carry out simulations in a box in proportion to the actual scale  
 233 (assuming that the dipole field is a reasonable approximation to the Earth’s magnetic  
 234 field at  $L \sim 5.6$ ), our simulation domain is accordingly placed at the dipole  $L$  value of  
 235 5.6. (In terms of the proton inertial length,  $\lambda_{p,\text{eq}} \equiv c/\omega_{pp,\text{eq}} = v_{A,\text{eq}}/\Omega_{cp,\text{eq}}$ , to which  
 236 MSWs are scaled,  $L = 770\lambda_{p,\text{eq}}/R_E$ .)

237 Due to the limited computational resources available, we use a reduced value for  
 238  $c/v_{A,\text{eq}} = 40$ , which increases our simulation time step ( $\Delta t$ ) drastically. For fixed  $n_{e,\text{eq}}$ ,  
 239 this is equivalent to the Earth’s dipole magnetic moment being one hundred times larger  
 240 than the actual value. However, it is important to point out that the relative field line  
 241 geometry is unchanged. In addition to the reduced  $c/v_{A,\text{eq}}$ , we utilize a reduced value  
 242 for the proton-to-electron mass ratio  $m_p/m_e = 100$  to alleviate the scale difference be-  
 243 tween electrons and ions. This leads to  $\omega_{pe,\text{eq}}/\Omega_{ce,\text{eq}} = (c/v_{A,\text{eq}})\sqrt{m_e/m_p} = 4$  in our  
 244 simulations (that is, we consider much heavier electrons).

245 Figure 2 shows a comparison between the cold plasma dispersion relations for  $\theta_{\mathbf{k}} =$   
 246  $90^\circ$  for the actual and reduced parameters. Note that while the proton inertial length  
 247 (to which the wavelength is scaled) is identical in both cases, the proton cyclotron fre-  
 248 quency (to which the wave frequency is scaled) is about thirteen times larger for the re-  
 249 duced parameters because of the increased dipole moment. The light orange region de-  
 250 notes the frequency range of the MSW event studied in Min, Liu, Wang, et al. (2018).  
 251 (It is also worth pointing out that statistically, wave power in the plasma trough is typ-  
 252 ically concentrated above 10th harmonic (Boardsen et al., 2016; Němec et al., 2015).)  
 253 For the present parameters which will be described shortly, our simulations cover the lower  
 254 end of the full MSW spectrum (Min & Liu, 2020), and longer wavelength modes.

#### 255 3.2 Initial Plasma Distribution

256 MSWs derive their energy from energetic protons having a ring-like velocity dis-  
 257 tribution with  $\partial f/\partial v_{\perp} > 0$ . There are several widely-used, analytical distribution func-  
 258 tions of this kind (e.g., Horne et al., 2000; Liu et al., 2011; Chen et al., 2018). Here, con-  
 259 sistent with our previous studies (Min, Liu, Wang, et al., 2018; Min, Liu, Denton, & Board-  
 260 sen, 2018; Min, Boardsen, et al., 2018; Min et al., 2019), we use the partial shell veloc-

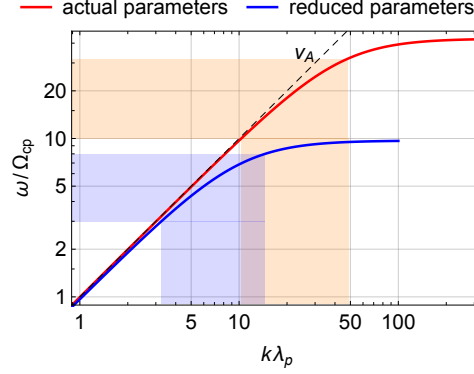


**Figure 2.** Comparison between the cold plasma dispersion relations for the actual (red) and reduced (blue) parameters (for  $\theta_{\mathbf{k}} = 90^\circ$ ). The light orange and blue shaded areas respectively denote the approximate frequency range of observed MSWs and the range where MSWs are excited in the present simulations.

ity distribution given by

$$f_{s,\text{eq}}(v, \alpha) = \frac{n_{s,\text{eq}}}{\pi^{3/2} \theta_s^3 C(v_s/\theta_s)} \exp\left(-\frac{(v - v_s)^2}{\theta_s^2}\right) \sin^{2A} \alpha, \quad (1)$$

where  $v = |\mathbf{v}|$  is the velocity modulus;  $\alpha$  is the pitch angle;  $A$  is the effective temperature anisotropy,  $A = T_\perp/T_\parallel - 1$ ;  $v_s$  and  $\theta_s$  are the ring (or shell) speed and the thermal spread of the shell, respectively;  $n_{s,\text{eq}}$  is the number density; and  $C(x)$  is the normalization constant given by

$$C(x) = \left[ x e^{-x^2} + \sqrt{\pi} \left( \frac{1}{2} + x^2 \right) \text{erfc}(-x) \right] \frac{\Gamma(1+A)}{\Gamma(3/2+A)}. \quad (2)$$

The subscript “eq” is to remind the readers that this partial shell distribution is described at the equator. Since according to Liouville’s theorem the distribution function is constant along the trajectory of representative particles, one can obtain the particle distributions anywhere along the field line (e.g., Roederer, 1970). Making use of the conservation of particle kinetic energy,  $KE = mv^2/2$ , and the magnetic moment,  $\mathcal{M} = mv_\perp^2/(2B)$ , one may get the velocity distribution mapped to latitude  $\lambda_{\text{lat}}$  (Xiao & Feng, 2006)

$$f_s(\lambda_{\text{lat}}; v, \alpha) = \frac{n_s(\lambda_{\text{lat}})}{\pi^{3/2} \theta_s^3 C(v_s/\theta_s)} \exp\left(-\frac{(v - v_s)^2}{\theta_s^2}\right) \sin^{2A} \alpha, \quad (3)$$

where we have defined the partial shell density  $n_s$  as

$$n_s(\lambda_{\text{lat}}) = n_{s,\text{eq}} \left( \frac{B_{\text{eq}}}{B(\lambda_{\text{lat}})} \right)^A. \quad (4)$$

Consequently, only the number density, but not the shape of the velocity distribution function, is dependent upon the field line coordinate. Here,  $B(\lambda_{\text{lat}}) = B_{\text{eq}} \sqrt{1 + 3 \sin^2 \lambda_{\text{lat}} / \cos^6 \lambda_{\text{lat}}}$  for the dipole magnetic field. The isotropic Maxwellian velocity distribution is recovered when  $v_s = 0$  and  $A = 0$ , for which the number density becomes constant along the field line.

For simplicity, we consider a three-component plasma consisting of a tenuous partial shell proton population (denoted by subscript  $s$ ), a dense isotropic background proton population (denoted by subscript  $p$ ), and a charge-neutralizing isotropic electron population (denoted by subscript  $e$ ). In the present simulations,  $n_{s,\text{eq}}/n_e = 0.025$ ,  $v_s =$

286  $1.7v_{A,\text{eq}}$ ,  $\theta_s = 0.43v_{A,\text{eq}}$ , and  $A = 0.5$ . Compared to our previous simulation studies,  
 287  $n_s$  is reduced by half in order to delay the growth time scale of MSWs. In addition, the  
 288 background proton and electron populations are assumed to be cold and their dynam-  
 289 ics are accordingly solved using the cold fluid approach (Tao, 2014). There are two rea-  
 290 sons for this hybrid approach. First, it helps reduce the computational cost and discrete  
 291 particle noise. Particularly, test simulations show that the background noise level is strongly  
 292 dependent on latitude (a larger noise level at higher latitude) when the background pop-  
 293 ulations are also treated kinetically. It turns out that keeping the noise level low at high  
 294 latitude is very important because the wave amplitudes there are low. Second, it has been  
 295 noticed that a parallel-propagating secondary mode develops in simulations when the  
 296 background populations are also treated kinetically. This mode also appeared in sim-  
 297 ulations of Min and Liu (2016) (see, e.g., Figure 7 therein), but we did not investigate  
 298 its cause at that time. After some tests, we concluded that this mode is unlikely driven  
 299 by the initially anisotropic partial shell distribution or the anisotropic background pro-  
 300 ton population at the later stage of simulation as a result of perpendicular heating. Rather,  
 301 it appears that some nonlinear effect involving the excited MSWs and the thermal back-  
 302 ground populations plays a role. Without a clear resolution at the moment and also due  
 303 to the noise concern, we decided to forgo the kinetic treatment of the background pop-  
 304 ulations and instead revisit this issue in a future study. On the other hand, the main role  
 305 of the background populations is, insofar as the present study is concerned, to support  
 306 wave propagation. So, using the hybrid approach, we take the kinetic effect of the back-  
 307 ground populations out of the picture and focus on the kinetic physics driven by the en-  
 308 ergetic partial shell protons. (For reference, the response of background populations were  
 309 discussed in Chen et al. (2018), Sun et al. (2017), and references therein.) Min and Liu  
 310 (2020) provides an extensive comparison between the linear theory analysis and simu-  
 311 lations using local plasma conditions at various latitudes, providing the validity and jus-  
 312 tification of our hybrid approach.

313 Before moving forward, we compare the present simulation parameters to Chen et  
 314 al. (2018)'s. Similar to our simulation parameters, Chen et al. (2018) used reduced val-  
 315 ues for  $m_p/m_e = 100$  and  $c/v_{A,\text{eq}} = 20$ . The center of their simulation domain, how-  
 316 ever, was located at  $L = 1$  (thus using the field line geometry at that location). They  
 317 also used a three-component electron-proton plasma including a charge-neutralizing elec-  
 318 tron population. The background proton and electron populations had a Maxwellian ve-  
 319 locity distribution with temperature equivalent to 1 eV, both of which were represented  
 320 as kinetic particles. For the energetic proton population that drives MSWs, they used  
 321 a Maxwellian-ring velocity distribution (see Chen et al., 2018, Eq. (2)) with a 5% con-  
 322 centration, ring speed  $V_R = v_{A,\text{eq}}$ , and the thermal spread of the ring  $w_{\text{pr}} = 0.141v_{A,\text{eq}}$   
 323 at the center of the simulation domain. The maximum temperature anisotropy at the  
 324 center was  $A_{\text{eq}} \approx 51$ , resulting in the free energy source contained well within  $\pm 10^\circ$  lat-  
 325 itude (see Figure 1). Despite the small (5%) concentration of the ring protons, the com-  
 326 bination of the large  $A_{\text{eq}}$  and the small thermal spread of the ring yielded a large max-  
 327 imum growth rate of about  $0.5\Omega_{cp,\text{eq}}$  at the center of the simulation domain.

### 328 3.3 Simulation Domain

329 Having determined the base parameters, we now describe the rest of the simula-  
 330 tion parameters.

331 Figures 3a–3b display the latitudinal dependence of some key parameters. The dipole  
 332 magnetic field  $B(\lambda_{\text{lat}})$  is almost three times larger at  $30^\circ$  latitude than  $B_{\text{eq}}$ . The Alfvén  
 333 speed profile  $v_A(\lambda_{\text{lat}})$  closely follows  $B(\lambda_{\text{lat}})$ , because partial shell protons (2.5% at most)  
 334 do not contribute significantly to the proton mass density. (Also, this means that the  
 335 proton inertial length is only weakly dependent on latitude,  $\lambda_p(\lambda_{\text{lat}}) \approx \lambda_{p,\text{eq}}$ .) Since the  
 336 absolute value for  $v_s$  is constant, the ratio  $v_s/v_A$ , which determines the unstable harmonic  
 337 frequency range of MSWs, is inversely proportional to  $v_A$ . This value drops below 0.7

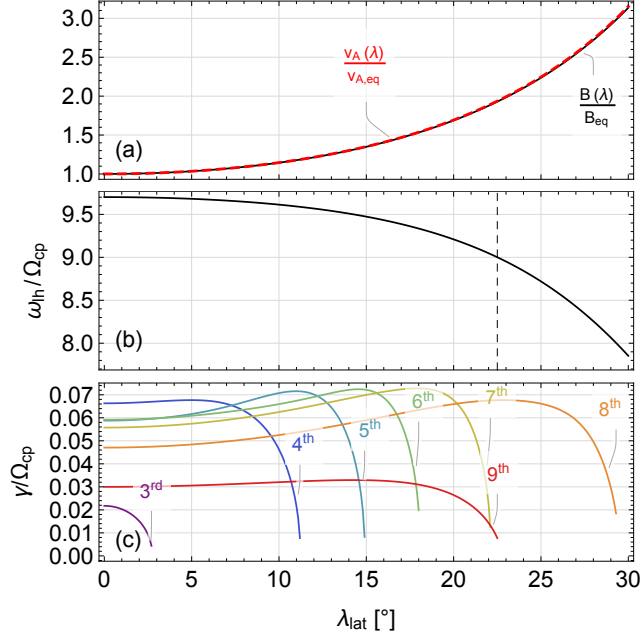


**Figure 3.** Latitudinal dependence of (a) the dipole magnetic field strength,  $B$  (black), and the Alfvén speed,  $v_A$  (red); and (b) the ratio of the lower hybrid frequency,  $\omega_{lh}$ , to the local proton cyclotron frequency,  $\Omega_{cp}$ . (c) Maximum growth rates (normalized by  $\Omega_{cp}$ ) at  $\theta_{\mathbf{k}} = 90^\circ$  versus latitude. Colors correspond to the different harmonics as labeled.

338 at about  $26^\circ$  latitude and above (see Min & Liu, 2020). The ratio of the lower hybrid  
 339 frequency,  $\omega_{lh}(\lambda_{\text{lat}})$ , to the local proton cyclotron frequency,  $\Omega_{cp}(\lambda_{\text{lat}})$ , on the other hand,  
 340 is related to the highest MSW harmonic mode that the system allows. This ratio (given  
 341 by  $\omega_{lh}/\Omega_{cp} = 1/\sqrt{v_A^2/c^2 + m_e/m_p}$ ) starts from just below 10 at the equator and mono-  
 342 tonically decreases with increasing latitude. Up until  $29^\circ$  latitude, there can be at least  
 343 eight harmonic modes. The transition of  $\omega_{lh}/\Omega_{cp}$  from above 9 to below is marked with  
 344 the vertical dashed line in Figure 3b drawn at  $22.5^\circ$  latitude. The simulated wave en-  
 345 ergy exhibits a sudden drop around this latitude (next section). Figure 3c shows the linear  
 346 growth rates at  $\theta_{\mathbf{k}} = 90^\circ$  calculated using the approximate formula given by Gulelmi  
 347 et al. (1975). Note that the growth rate,  $\gamma$ , is normalized by  $\Omega_{cp}$ . Because the maximum  
 348 value of  $\gamma/\Omega_{cp}$  over all harmonics is  $\sim 0.07$  up to about  $27^\circ$  latitude and  $\Omega_{cp}$  increases  
 349 with latitude, MSWs actually grow fastest initially near  $25^\circ$  latitude (Min & Liu, 2020,  
 350 Figure 1).

351 Based on the above analysis, using latitudinal boundaries at about  $\pm 30^\circ$  latitude  
 352 should be sufficient. Figure 4a displays a three-dimensional rendering of the simulation  
 353 box (red outline). We set the simulation grid sizes at the equator as  $r_0 \Delta\phi \times \Delta s = 0.05\lambda_p \times$   
 354  $0.5\lambda_p$ , where  $\phi$  is the azimuthal coordinate,  $ds = r_0 \cos \lambda_{\text{lat}} \sqrt{4 - 3 \cos^2 \lambda_{\text{lat}}} d\lambda_{\text{lat}}$  is the  
 355 dipole field line arc length, and  $r_0 = LR_E$  is the equatorial distance from the Earth center  
 356 to the field line. The field line grid spacing increases with latitude proportional to  
 357  $B(\lambda_{\text{lat}})$  to keep the flux tube volume roughly constant (Hu & Denton, 2009). The grid  
 358 spacing at the equator is small enough to resolve wave numbers up to  $k_{\parallel} = 2\pi/\lambda_p$  along  
 359 the field line and up to  $k_{\perp} = 20\pi/\lambda_p$  in the azimuthal direction. (Note that  $k_{\perp}$  of the  
 360 largest (9th) harmonic is about  $30\lambda_p^{-1}$  (Min & Liu, 2020, Figure 4).) The number of the  
 361 grid points is  $N_{\phi} \times N_{\lambda_{\text{lat}}} = 480 \times 1200$ . The length of the simulation domain in the  
 362 azimuthal direction ( $N_{\phi} \Delta\phi = 1.8^\circ$ ) is sufficient to resolve the longest MSWs (about  
 363 4 wave cycles for the fundamental mode at the equator). The simulation time step is  $\Delta t =$

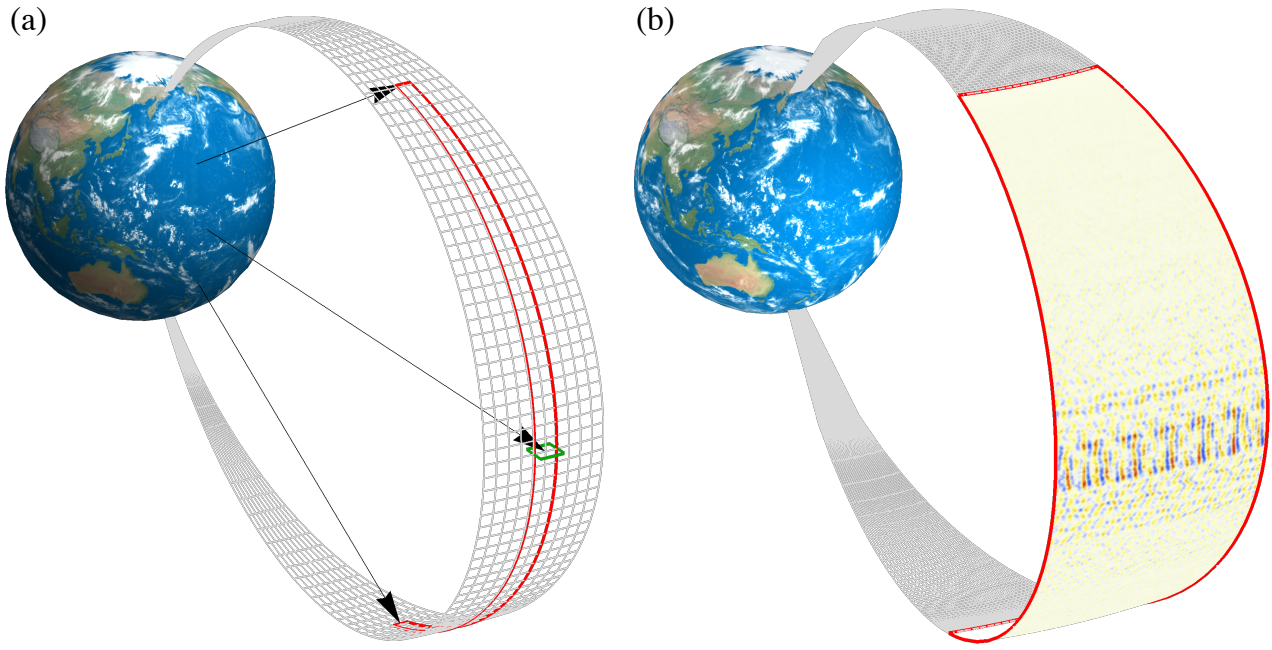


**Figure 4.** (a) Three-dimensional rendering of the constant  $L$ -shell surface (gray mesh) and the outline of the present simulation domain (red). The green box at the equator for comparison denotes the simulation box used in Min, Liu, Denton, and Boardsen (2018). (b) Three-dimensional rendering of the azimuthal component of the simulated electric field,  $\delta E_\phi$ , at  $t\Omega_{cp,eq} = 130$ . The azimuthal dimension has been stretched by a factor of ten to display the wave field structure. (Earth globe texture provided courtesy of Tom Patterson, [www.shadedrelief.com](http://www.shadedrelief.com).)

364  $0.0005\Omega_{cp,eq}^{-1}$ . Since the azimuthal extent of the source region is typically much larger than  
 365 the radial extent, the periodic boundary conditions in the azimuthal direction may be  
 366 appropriate. In contrast, absorbing boundary conditions are used in the latitudinal bound-  
 367 aries to damp out the outgoing waves (Umeda et al., 2001), although most of MSWs ex-  
 368 cited in the system are refracted toward the equator before reaching the latitudinal bound-  
 369 aries (section 4). Since the width of each absorbing layer is 20 grid points wide, the phys-  
 370 ical domain size in the field line direction is actually 1160 grid points wide (or equiva-  
 371 lently  $\lambda_{lat} \approx \pm 27^\circ$ ). The number of the simulation particles for the energetic partial  
 372 shell proton population is on average 2,500 per cell at the magnetic equator and decreases  
 373 with magnetic latitude proportional to  $n_s(\lambda_{lat})$  (which means there are about  $2,500 \times$   
 374  $0.56 = 1,400$  simulation particles per cell at  $30^\circ$  latitude). As will be shown, we be-  
 375 lieve that (together with test simulations not shown here) the small amount of scatter-  
 376 ing of the partial shell protons shown in Figure 11f is a sign of convergence. Note that  
 377 the simulation particles reaching the latitudinal boundaries are reflected back into the  
 378 simulation domain, including those within the loss cone. This is not the most accurate  
 379 description, but the fact that the transport of ring/shell protons into the loss cone due  
 380 to the scattering by excited MSWs is very minimal (e.g., Liu et al., 2011, Figure 8) in-  
 381 dicates that this description is nevertheless reasonable.

## 382 4 Simulation Results

383 Figure 4b displays a three-dimensional rendering of the simulated electric field fluctua-  
 384 tions,  $\delta E_\phi$ , around the time of wave energy saturation (see Figure 5a). (The azimuthal  
 385 dimension has been stretched by a factor of ten to visualize the azimuthal wave struc-  
 386 ture.) To effectively convey the main results of the present simulation, we focus on the  
 387 presentation of latitude-time wave intensity distribution to investigate the global evo-  
 388 lution of MSWs; spatial and temporal power spectrograms to investigate wave spectral  
 389 properties; and the energetic proton distribution function to investigate the evolution  
 390 of free energy.

### 391 4.1 Wave Energy and Poynting Flux

392 Figures 5a and 5b show fluctuating electric and magnetic field intensity,  $\langle \delta E^2 \rangle_\phi$  and  
 393  $\langle \delta B^2 \rangle_\phi$ , as a function of time and field line coordinate, where the angled bracket means  
 394 average over the azimuthal grid points,  $\langle \cdot \rangle_\phi = \frac{1}{N_\phi} \sum_{i=1}^{N_\phi}$ . The upper tick marks indi-  
 395 cate magnetic latitude, and the color bar scale is linear. First of all, both the electric field  
 396 and magnetic field exhibit maximum intensity near the equator around  $t\Omega_{cp,eq} = 150$ ,  
 397 indicated by the rectangular box labeled “A”. The box spans  $\pm 6^\circ$  in latitude, so the wave  
 398 energy is roughly contained within this range. Before reaching the maximum intensity,  
 399 the faint streak-like pattern merges toward the equator as if waves have been propagated  
 400 toward the equator. It is not clear at this point how much the waves excited off the equa-  
 401 tor contribute to the intensity peak at the equator. One can anticipate that if the waves  
 402 excited near the equator are the main contributor, the frequency spectrum will exhibit  
 403 discrete harmonic peaks and the average normal angle will be close to  $90^\circ$  (see Min &  
 404 Liu, 2020). If, on the other hand, the off-equatorial waves are the main contributor, the  
 405 average value for  $\theta_k$  will become smaller due to the spread in the wave normal angle dis-  
 406 tribution and the discrete harmonic pattern will be less pronounced due to superposi-  
 407 tion of MSWs from multiple sources at different latitudes. We will show in the next sec-  
 408 tion that the waves contained in box “A” are mainly from the equatorial source.

409 After wave intensity has reached the primary maximum around  $t\Omega_{cp,eq} = 150$ , there  
 410 appears a secondary enhancement starting from  $t\Omega_{p,eq} \approx 200$ . It extends over a much  
 411 broader latitudinal range as indicated by the box labeled “B2”. Although only one box  
 412 in the southern hemisphere is drawn, the system is symmetric about the equator and the  
 413 same process is mirrored to the other hemisphere. This secondary enhancement is more

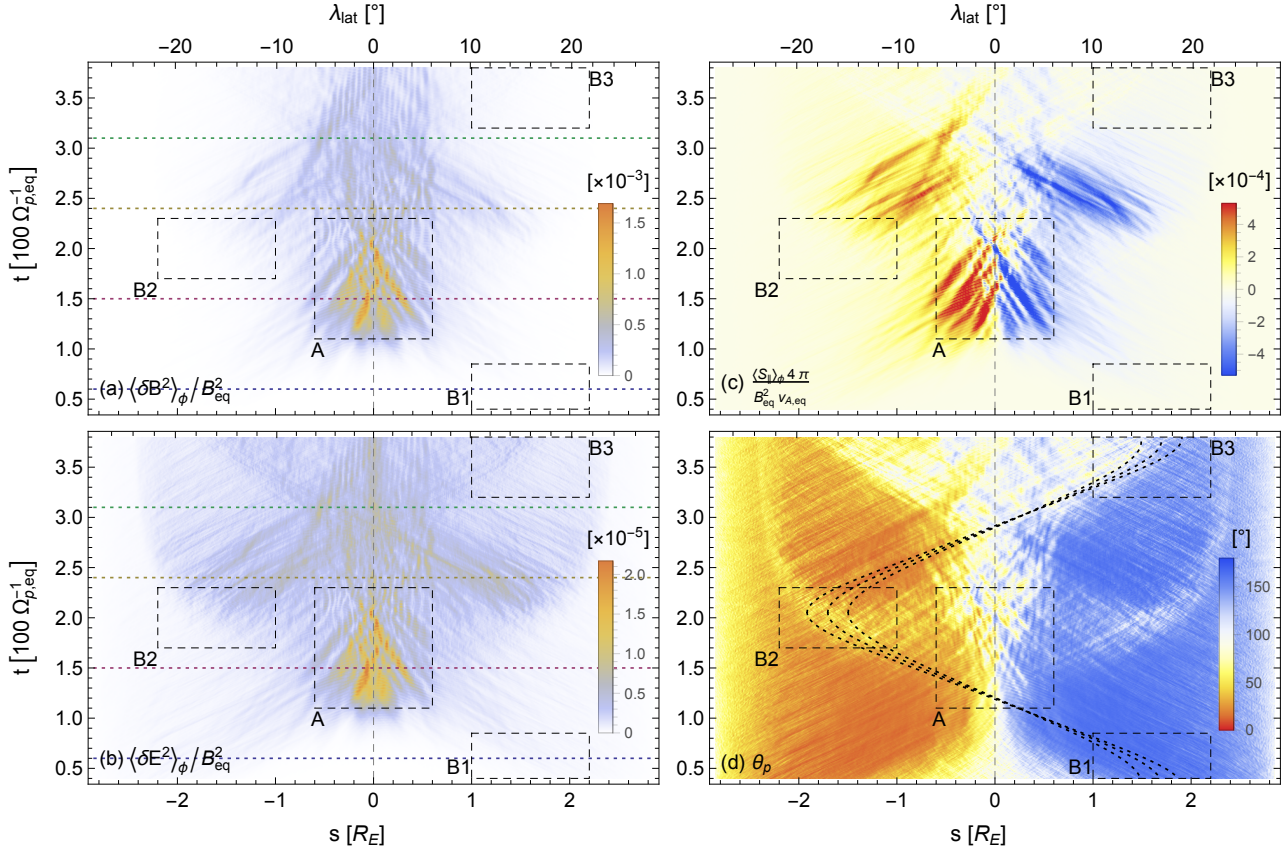


**Figure 5.** (a–b) Two-dimensional color plots of (a) magnetic,  $\langle \delta B^2 \rangle_\phi$ , and (b) electric,  $\langle \delta E^2 \rangle_\phi$ , field intensity as a function of time and field line coordinate (or magnetic latitude). The color scale is linear, and  $\langle \cdot \rangle_\phi$  means averaging over the azimuthal grid points. Energy is normalized by  $B_{\text{eq}}^2$ . (c) Parallel component of the Poynting flux,  $\langle S_{\parallel} \rangle_\phi$ , as a function of time and field line coordinate (or magnetic latitude). The Poynting flux is normalized by  $B_{\text{eq}}^2 v_{A,\text{eq}} / 4\pi$ . (d) Poynting vector angle,  $\theta_p = \cos^{-1}(\langle S_{\parallel} \rangle_\phi / \langle |\mathbf{S}| \rangle_\phi)$ . The color map is chosen to match that of (c): Reddish and bluish color means Poynting vector directions northward and southward, respectively. The three dotted curves superimposed are the trajectories of sample rays of the 8th harmonic.

pronounced in  $\langle \delta E^2 \rangle_\phi$  due in part to the fact that the wave frequency gets closer to  $\omega_{lh}$  and MSWs become more electrostatic in nature. In Figure 5b, the streak-like pattern clearly indicates that the waves excited in a wide latitudinal extent subsequently propagate toward the equator and then to the opposite hemispheres. Near the end of the run, the waves that have reached the opposite hemispheres experience a refraction and subsequently propagate toward the equator (refer to the region outlined by the box labeled “B3”; and also Figure S6b).

Based on these observations, we may group the waves in the simulation into two. The first group involves the waves that contribute to the primary intensity maximum at the early stage of the simulation (box “A”) and decay afterward. The waves in this group remain near the equatorial region throughout the run (well contained within the latitudinal extent of box “A”) and form the standing-wave pattern after  $t\Omega_{cp,eq} \gtrsim 240$ . The waves in the second group, in contrast, occupy a larger latitudinal extent (but with lower intensity) and are more dynamic in that they bounce back and forth between two conjugate hemispheres, as often shown in ray tracing studies. It appears that the initial waves excited around box “B1” travel to box “B2” in the opposite hemisphere where they experience refraction and subsequently pick up more energy (or they provide the seed fluctuations for the secondary enhancement), and then bounce back to box “B3”. (Note that these wave packets also move in the azimuthal direction, and probably in the radial direction as well in the full three-dimensional case.) By symmetry, the waves starting at the southern hemisphere will go through the same process but in the opposite direction. We will present supporting evidence for this interpretation in the rest of the paper.

Figure 5c shows the parallel component of the Poynting flux averaged over the azimuthal grid points,  $\langle S_{\parallel} \rangle_\phi$ . The bluish and reddish colors indicate propagation northward ( $S_{\parallel} > 0$ ) and southward ( $S_{\parallel} < 0$ ), respectively. The double-peaked wave intensity structure in time is also shown in  $\langle S_{\parallel} \rangle_\phi$  (one at around  $t\Omega_{cp,eq} = 150$  and the other at around  $t\Omega_{cp,eq} = 250$ ). More interestingly, the direction of the Poynting vector is dominantly equatorward such that it points northward (southward) at the southern (northern) hemisphere. Nevertheless, the signatures of poleward Poynting flux is sparsely shown. For example, within boxes “A” and “B3” in Figure 5d, wave packets originating from the opposite hemispheres maintain substantial intensity so that they leave the trace of poleward Poynting flux.

Figure 5d shows the angle,  $\theta_p$ , between the Poynting vector and the dipole magnetic field vector. (Note that  $\theta_p$  is not the same as the wave normal angle,  $\theta_k$ .) The color map is reversed to match the directionality of Figure 5c. The main purpose of the  $\theta_p$  plot is to highlight the trajectories of simulated wave packets. We have calculated sample ray trajectories using the formulae given by Shklyar and Balikhin (2017). Superimposed in Figure 5d are three sample trajectories of the 8th harmonic traced forward and backward in time starting from  $-19$ ,  $-17$ , and  $-15^\circ$  latitudes centered at  $t\Omega_{cp,eq} = 210$  (inside box “B2”). All rays initially had  $\theta_k = 90^\circ$ . Evidently, the streak-like pattern is aligned quite well with these sample ray paths. (We note that reducing discrete particle noise is particularly important to observe the bouncing wave signature.) For reference, the sample rays traveled approximately  $0.6R_E$  (or about  $6.5^\circ$ ) in the azimuthal direction during half a bounce period, which is a bigger distance than the azimuthal length of the simulation box ( $1.8^\circ$  wide).

An interesting feature that stands out in Figure 5b is the sudden drop-off in intensity for  $t\Omega_{cp,eq} \gtrsim 250$  and at  $|\lambda_{lat}| \approx 22.5^\circ$ . The border in  $\lambda_{lat}$  is more clearly shown in Figure 5b. This latitude coincides with where  $\omega_{lh}/\Omega_{cp}$  transitions from above 9 to below shown in Figure 3b. Without definitive proof, we surmise that this drop-off in wave energy is related to the sudden disappearance of the 9th harmonic mode above  $|\lambda_{lat}| \approx 22.5^\circ$ .

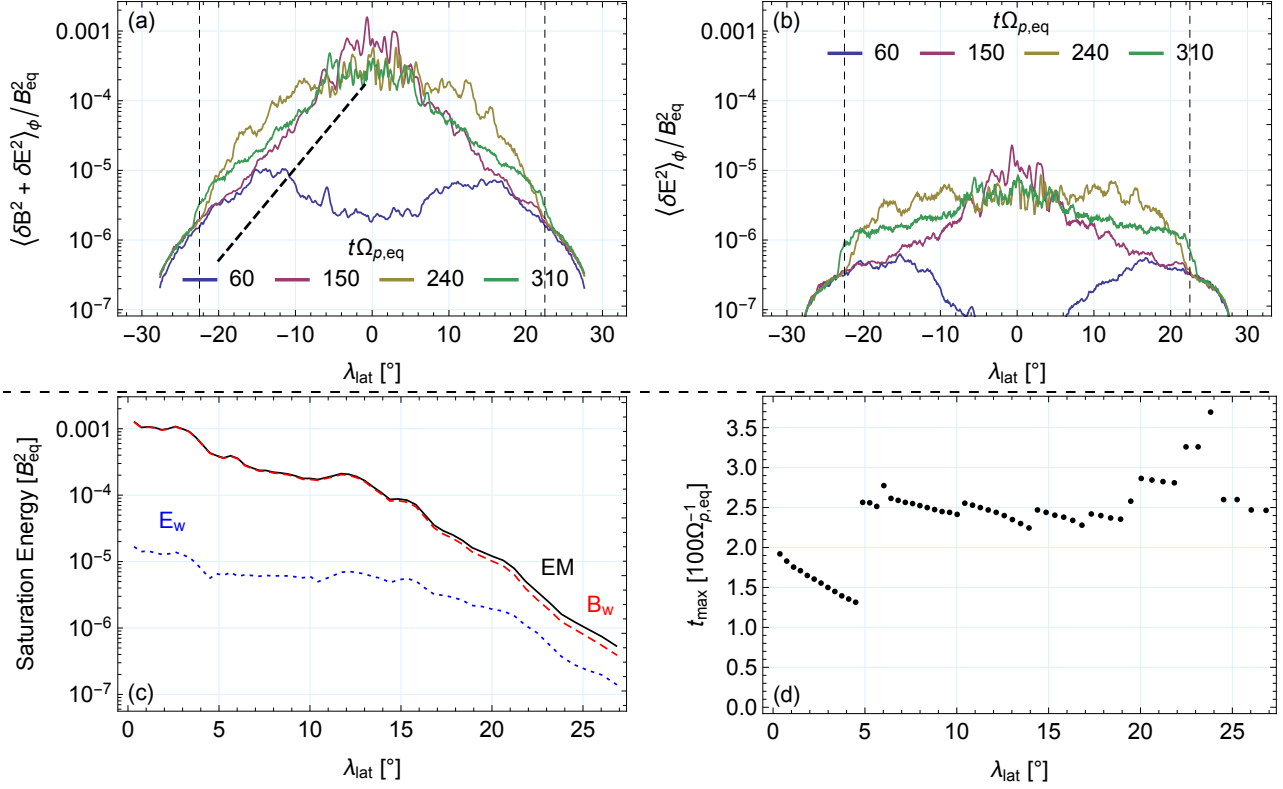


**Figure 6.** (a) Total wave intensity,  $\langle \delta B^2 + \delta E^2 \rangle_\phi$ , as a function of latitude at the times labeled (also indicated by horizontal dashed lines of the same colors in Figures 5a and 5b). The dashed line in the southern hemisphere of Figure 6a is an exponential fit to the curve at  $t\Omega_{p,\text{eq}} = 150$  with an e-folding value of 0.3. (b) Electric field wave intensity,  $\langle \delta E^2 \rangle_\phi$ , as a function of latitude at the same times. The vertical dashed lines are drawn at  $\pm 22.5^\circ$  latitudes. (c) Maximum wave intensity (or saturation energy) at a given latitude. The labels B<sub>w</sub>, E<sub>w</sub>, and EM denote the magnetic, electric, and total wave intensity, respectively; and (d) the time of saturation at a given latitude.

Figure 6 presents the detailed latitudinal variation of wave intensity, which may be compared with observational data. Figures 6a and 6b show  $\langle \delta B^2 + \delta E^2 \rangle_\phi$  and  $\langle \delta E^2 \rangle_\phi$ , respectively, at  $t\Omega_{cp,eq} = 60, 150, 240,$  and  $310$ . Before the primary maximum intensity is reached at  $t\Omega_{cp,eq} \approx 150$ , the latitudinal profile exhibits a local minimum in intensity at the equator and two maxima off the equator, indicating that the excitation actually starts first at high latitude. As time goes on, these two maxima move toward the equator to form a single maximum at the equator, as shown in Figures 5a and 5b. Approximately at  $t\Omega_{cp,eq} = 150$ , the primary maximum in intensity is reached. As suggested earlier, the wave energy is contained well within  $\pm 10^\circ$  latitude, because the difference in intensity is more than an order of magnitude. More quantitatively, the dashed line superimposed in Figure 6a is an exponential fit ( $\sim e^{-a|\lambda_{lat}|}$ ) to the  $t\Omega_{cp,eq} = 150$  profile (purple curve) with an e-folding value of approximately 0.3. Subsequently, a secondary enhancement off the equator reaches its maximum in intensity around  $t\Omega_{cp,eq} = 240$ . Because the waves near the equator have decayed away slightly by this time, the intensity profile exhibits a broader peak extending beyond  $|\lambda_{lat}| = 10^\circ$ . Although the intensity as a function of latitude no longer exhibits the exponential behavior, an exponential fit suggests an e-folding value of about 0.16. Finally, the green curve shows the intensity profile at  $t\Omega_{cp,eq} = 310$  at which time many of the off-equatorial waves have converged at the equator. Consequently, the e-folding value increases again to approximately 0.21. As one can see, the contribution of the electric field to the total wave energy is negligible for  $\lambda_{lat} \lesssim 20^\circ$  at all times.

In Figure 6c, the maximum wave intensities at given latitudes are plotted versus latitude. A rectangular box ( $5\Omega_{cp,eq}^{-1}$  long in time and 20 grid points wide in latitude) smoothing is applied to Figures 5a and 5b prior to this analysis. This can be compared with the local simulation results by Min and Liu (2020, Figure 2). The large drop in intensity at high latitude indicates that MSWs are not efficiently tapping into the free energy there. As soon as a wave starts growing, it is refracted equatorward due (mainly) to the gradient of the background magnetic field (see the sample rays in Figure 5d) and thus moves out of the region where the growth rate is positive (e.g., Boardsen et al., 2016). On the other hand, the latitudinal dependence of the relative strength between the electric and magnetic fields is largely consistent with the local simulation results. Figure 6d plots the time when the maximum values (saturation times) were taken. Focusing on  $\lambda_{lat} \lesssim 20^\circ$ , the times when the maximum values are reached are consistent with the two-group-wave interpretation mentioned earlier.

## 4.2 Wave Field Structure and Frequency Spectrum

This subsection describes the spatial wave field structure and the power spectral density distribution in frequency and wave number space.

Figure 7 shows two snapshots of  $\delta E_\phi$  at  $t\Omega_{p,eq} = 150$  and  $240$  in  $(\phi, s)$  coordinate space. Note that the dipole magnetic field is parallel to the vertical axis and perpendicular to the horizontal axis. The wave fronts are much more complex than those in Chen et al. (2018); part of the reason is that waves propagating left and right are mixed together due to the periodic boundary conditions used in the azimuthal direction, forming the criss-cross pattern of wave fronts. Nevertheless, one may appreciate that the wave fronts are relatively vertical in the vicinity of the equator (between the two horizontal dashed lines drawn at  $\lambda_{lat} = \pm 4^\circ$ ), especially during the primary wave intensity maximum (Figure 7a), and become quickly oblique outside. Movies included in supporting information show that propagation of MSWs is dominantly in the azimuthal direction (i.e., quasi-perpendicular to the dipole magnetic field). Also, consistent with the Poynting flux shown in Figure 5c, MSWs off the equator converge toward the equator, and eventually propagate to the opposite hemispheres near the end of the simulation.

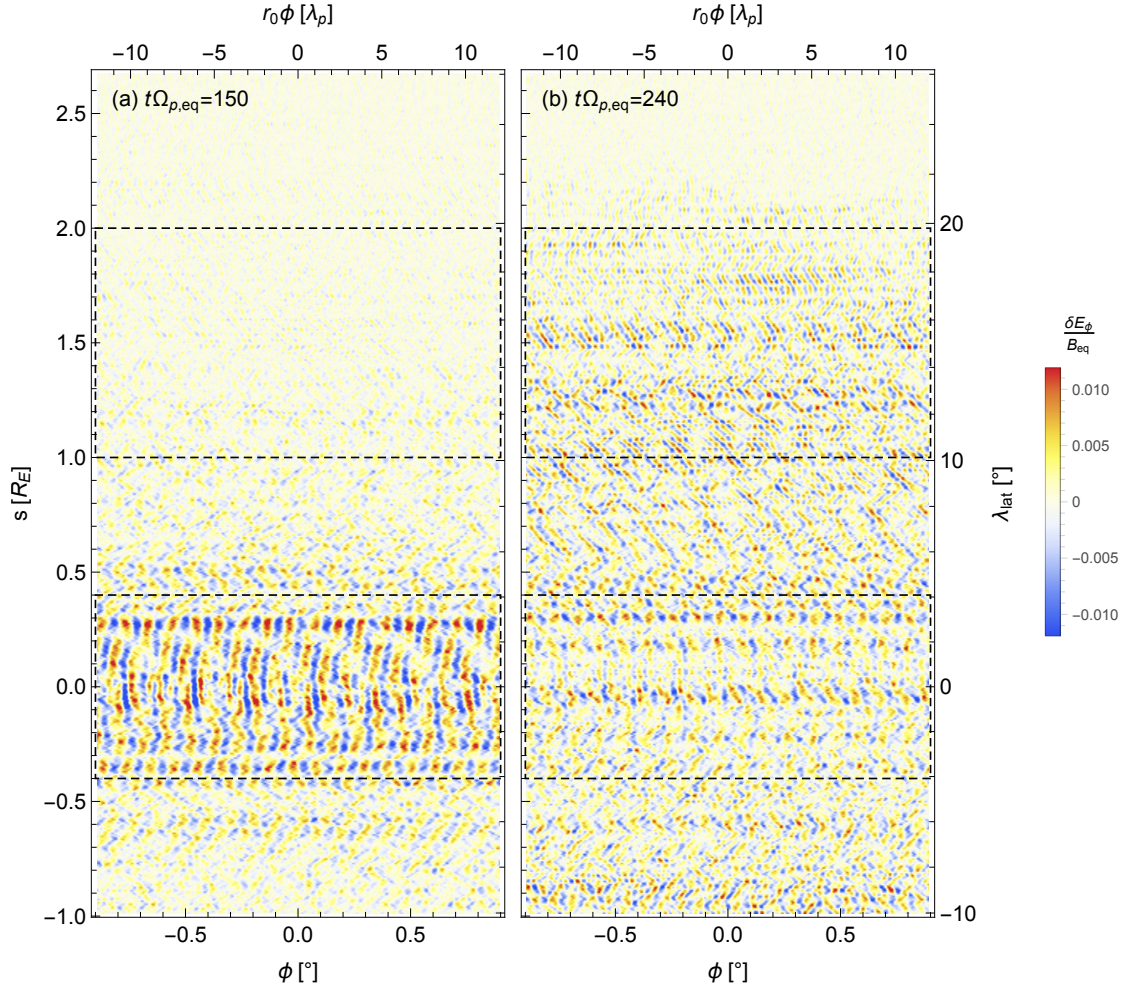


**Figure 7.** Snapshots of  $\delta E_\phi$  at  $t_{\Omega_{p,eq}} = 150$  and  $240$  displayed in  $(\phi, s)$  coordinate space. In addition, the right axis displays magnetic latitude, and the top axis displays  $r_0\phi$  in units of the proton inertial length,  $\lambda_p$ .

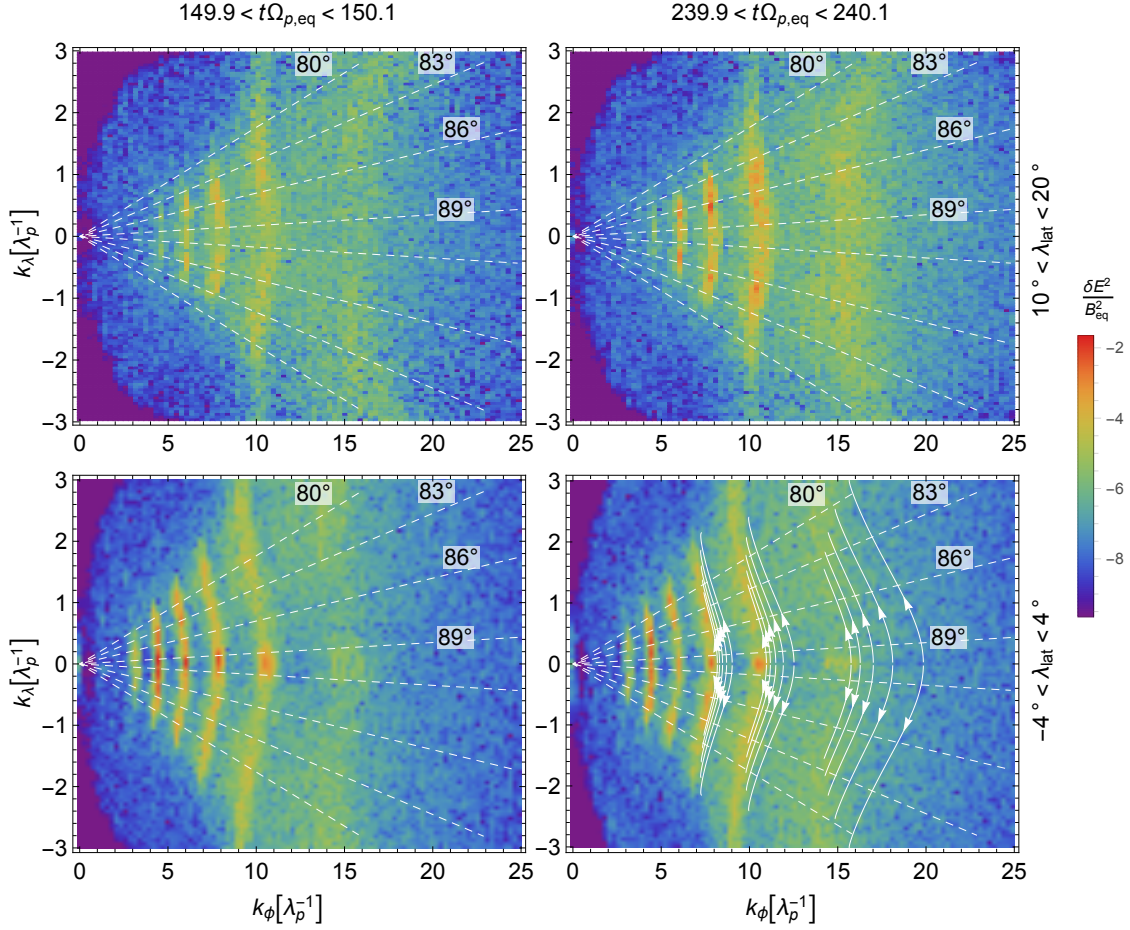


**Figure 8.** Electric field power spectral density in wave number space. The corresponding latitudinal extent and time are displayed at the top and right axes of the panels. The parallel ( $k_\lambda$ ) and perpendicular ( $k_\phi$ ) wave numbers are normalized to the proton inertial length,  $\lambda_p$ . The harmonic numbers can be identified as follows: the outermost discrete mode at  $k_\phi \lambda_p \approx 15$  is the 8th harmonic mode, and one can count from there one by one toward smaller  $k_\phi$ . The dashed lines radiating from the origin correspond to  $\theta_{\mathbf{k}} = 80, 83, 86,$  and  $89^\circ$  as labeled. The white curves in the lower-right panel are paths of sample rays in wave number space corresponding to the 6th, 7th, and 8th harmonics. For each harmonic, five rays were traced starting from  $15, 17, 19, 21,$  and  $23^\circ$  latitudes (from the leftmost to rightmost curves) with an initial wave normal angle  $\theta_{\mathbf{k}} = 90^\circ$ . Tracing ended when the rays arrived at the equator.

516 To get a more quantitative understanding of the wave power distribution in  $\theta_{\mathbf{k}}$  space,  
 517 we took a Fourier transform of the simulated wave fields in two latitudinal ranges of  $-4^\circ <$   
 518  $\lambda_{\text{lat}} < 4^\circ$  and  $10^\circ < \lambda_{\text{lat}} < 20^\circ$ , as marked by the horizontal dashed lines in Figure 7.  
 519 The result is shown in Figure 8. For reference, Min and Liu (2020, Figure 4) shows the  
 520 linear instability growth rates and the wave spectral densities from local two-dimensional  
 521 simulations, where in comparison with Figure 8 wave power is concentrated closer to the  
 522  $90^\circ$  wave normal angle, especially in the equatorial region. Wave power in the present  
 523 simulation spans up to the  $\theta_{\mathbf{k}} = 80^\circ$  marks at around  $15^\circ$  latitudes, and beyond  $\theta_{\mathbf{k}} =$   
 524  $77^\circ$  around the equator. The major difference between the equatorial and off-equatorial  
 525 waves is the pronounced presence of quasi-perpendicular propagating modes (within the  
 526  $\theta_{\mathbf{k}} = 89^\circ$  marks). At the equator, there are isolated peaks in wave power at  $\theta_{\mathbf{k}} \approx 90^\circ$   
 527 essentially for all harmonics, whereas there is a local minimum of wave power at  $\theta_{\mathbf{k}} =$   
 528  $90^\circ$  in the latitudinal range of  $10^\circ < \lambda_{\text{lat}} < 20^\circ$ . (In comparison, the local simulations  
 529 of Min and Liu (2020) produced dominant wave power at  $\theta_{\mathbf{k}} = 90^\circ$  in this latitudinal  
 530 range). The power-weighted average wave normal angle at  $t\Omega_{cp,eq} = 150$  is about  $\theta_{\mathbf{k}} =$   
 531  $87^\circ$  at the equatorial region and  $\theta_{\mathbf{k}} = 85^\circ$  in the latitudinal range of  $10^\circ < \lambda_{\text{lat}} < 20^\circ$ .  
 532 Due to the wide spread of power in  $\theta_{\mathbf{k}}$  space at the equator, the difference is actually only  
 533 a few degrees at most. At the later time, the average  $\theta_{\mathbf{k}}$  values are  $85^\circ$  at the equator  
 534 and  $86^\circ$  in the latitudinal range of  $10^\circ < \lambda_{\text{lat}} < 20^\circ$ . Also, it should be noted that the  
 535 power-weighted average wave normal angle near the equatorial region will vary depend-  
 536 ing on the size of the latitudinal range we choose.

537 To better understand the spectral pattern and the origin of the wave modes at  $\theta_{\mathbf{k}} \lesssim$   
 538  $86^\circ$  not predicted by the local linear theory analysis, the trajectories of sample rays are  
 539 superimposed in the lower-right panel of Figure 8. Three groups of rays corresponding  
 540 to the 6th, 7th, and 8th harmonics, respectively, were traced. In each group, five rays  
 541 were launched from 15, 17, 19, 21, and  $23^\circ$  latitudes (from the leftmost to rightmost curves  
 542 in each ray bundle) with an initial wave normal angle  $\theta_{\mathbf{k}} = 90^\circ$ . We chose the  $90^\circ$  wave  
 543 normal angle for simplicity, because the growth rate maximizes at  $\theta_{\mathbf{k}} \gtrsim 88^\circ$  (Min & Liu,  
 544 2020). Tracing ended when the rays arrived at the equator. The locations where the rays  
 545 landed in wave number space line up quite well with the strips of enhanced power, in-  
 546 dicated their off-equatorial origin. In contrast, the waves at  $\theta_{\mathbf{k}} = 90^\circ$  do not connect  
 547 to any off-equatorial rays, hence consistent with the interpretation that they were gen-  
 548 erated locally.

549 Figure 9 shows short-time frequency spectrograms at 0, 5, 10, and  $15^\circ$  latitudes,  
 550 which are more relevant to observational data analyses. The window size is around  $42\Omega_{cp,eq}^{-1}$   
 551 long. At the equator, there are multiple discrete spectral peaks, on top of a weaker, more  
 552 continuous spectrum extending beyond  $\omega_{lh}$ . The discrete spectral peaks are found at har-  
 553 monics of  $\Omega_{cp}$  (from 3rd to 7th by visual inspection; see the vertical scale on the right  
 554 side of the panel), indicating that they have been excited locally. On the other hand, the  
 555 waves corresponding to the continuous spectrum should have their source off the equa-  
 556 tor. The relative strength of the discrete modes (i.e., of the local origin) compared to  
 557 the continuous mode (i.e., of the off-equator origin) decreases with increasing latitude,  
 558 and at  $15^\circ$  latitude only the 5th harmonic (which is the fastest growing mode at that  
 559 latitude (see Min & Liu, 2020, Figure 4)) is barely seen (see the vertical scale on the right  
 560 side of the panels). Hence, the continuous spectrum dominates there.

561 Some studies analyzed the frequency-latitude dependent wave power distributions.  
 562 We can of course deploy virtual satellites along a field line in the simulation to capture  
 563 time-series of electric and magnetic fields. Figure 10 shows the electric and magnetic field  
 564 spectrograms within two temporal spans,  $118.6 < t\Omega_{cp,eq} < 181.4$  and  $208.6 < t\Omega_{cp,eq} <$   
 565  $271.4$ . For guidance, the white dashed curves denote integer multiples of  $\Omega_{cp}$ , and the  
 566 black dotted curves indicate  $\omega_{lh}/\Omega_{cp}$ . One can immediately see that the latitude at which  
 567 a given harmonic mode disappears below the noise level is an increasing function of the  
 568 harmonic number. This is approximately consistent with the latitude at which the growth

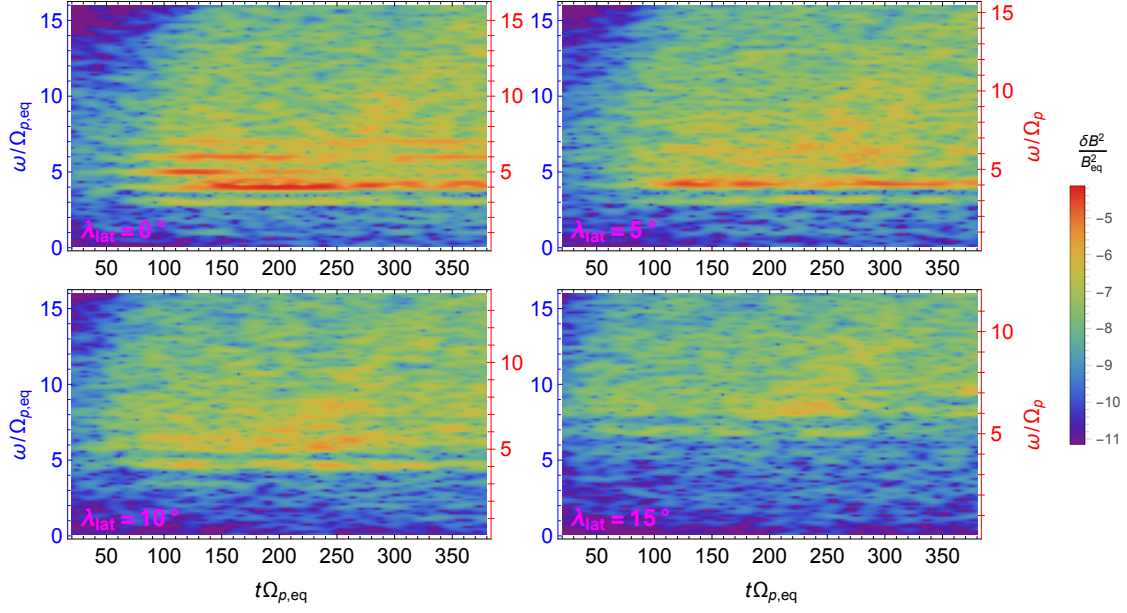


**Figure 9.** Short-time frequency spectrograms of the fluctuating magnetic field at 0, 5, 10, and 15° latitudes. In each panel, the left blue tick marks denote frequency normalized by  $\Omega_{cp,eq}$ , and the right red tick marks denote frequency normalized by  $\Omega_{cp}$ , the local proton cyclotron frequency.

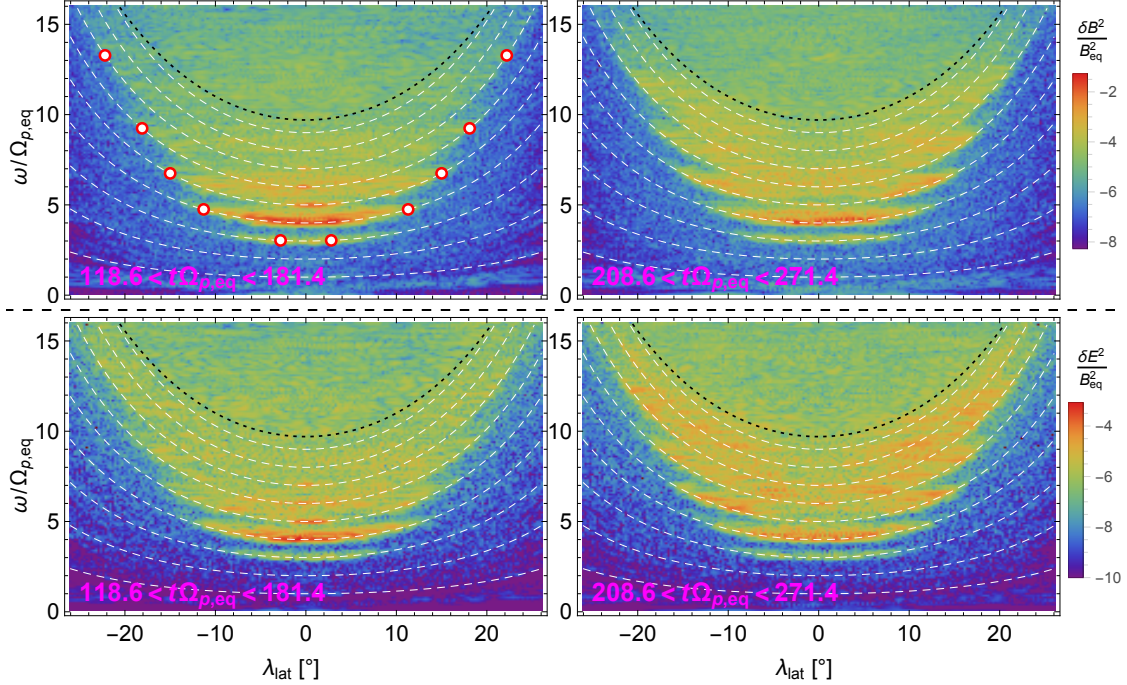


**Figure 10.** Frequency-latitude power spectral densities of the fluctuating magnetic field (top) and electric field (bottom). The left and right columns correspond to two different time spans,  $118.6 < t\Omega_{cp,eq} < 181.4$  and  $208.6 < t\Omega_{cp,eq} < 271.4$ , respectively. For guidance, the white dashed curves denote integer multiples of  $\Omega_{cp}$ , and the black dotted curves indicate  $\omega_{lh}/\Omega_{cp}$ . The red open circles in the top-left panel mark the latitudes at which the growth rates of the various harmonic modes shown in Figure 3c turn negative.

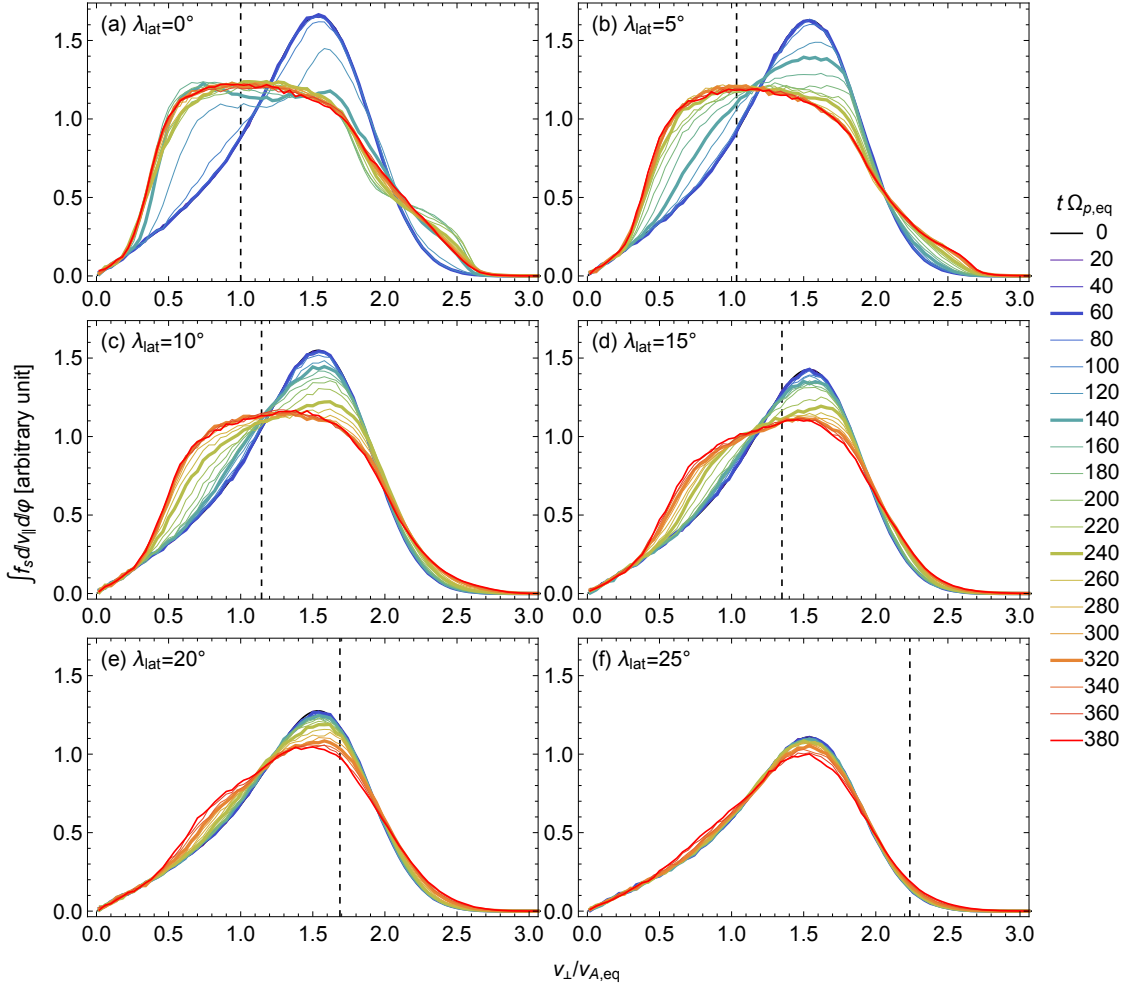


**Figure 11.** Temporal evolution of the energetic partial shell proton distributions sampled at latitudes  $\lambda_{\text{lat}} = 0, 5, 10, 15, 20,$  and  $25^\circ$ . Line color denotes times as labeled, with the thicker lines approximately corresponding to the time slices in Figures 6a and 6b. The vertical dashed lines mark the local Alfvén speed,  $v_A$ .

569 rates of the corresponding harmonics become negative as indicated by the open circles  
 570 in the top-left panel. Note that such a behavior is related to the varying  $v_s/v_A$  ratio at  
 571 different latitude as well as equatorward propagation of MSWs excited near the harmon-  
 572 ics of  $\Omega_{cp}$  (manifested as diffuse wave power in frequency space). Although the reduced  
 573  $m_p/m_e$  and  $c/v_{A,\text{eq}}$  used in our simulation limit MSWs to a narrower frequency range  
 574 than observed, the outline of the spectral power in latitude-frequency space resembles  
 575 the funnel-shaped spectrograms discussed by Boardsen et al. (1992, 2016). In addition,  
 576 it is only the low frequency part of the spectrum near the equator that exhibits discrete  
 577 spectral peaks.

### 578 4.3 Evolution of Partial Shell Proton Distribution

579 In this section, we examine the temporal evolution of energetic partial shell pro-  
 580 tons along the field line. Figure 11 shows the reduced velocity distribution functions,  $\int_{-\infty}^{\infty} \int_0^{2\pi} f_s d\phi dv_{\parallel}$ ,  
 581 as a function of the perpendicular velocity,  $v_{\perp}$ , sampled at several different latitudes. (For  
 582 reference, the reduced distribution functions from local two-dimensional simulations (Min

583 & Liu, 2020) are included in the supporting information, Figure S5.) The excited MSWs  
 584 scatter the protons to reduce the positive slope (and also the negative slope beyond the  
 585 peak of the initial distribution) of the energetic partial shell proton distribution func-  
 586 tions in a wide latitudinal range. The degree to which the scattering occurs is strongly  
 587 dependent upon latitude. The distribution function at  $25^\circ$  latitude has barely changed  
 588 (cf. Figure S5), whereas energetic protons near the equator experienced the largest scat-  
 589 tering. Interestingly (but not surprisingly), this trend has a correlation with the local  
 590 wave intensity shown in Figures 5a and 5b. The evolution of the distribution function  
 591 at the equator is pretty much finished between  $60 < t\Omega_{cp,eq} < 140$ , during which ex-  
 592ponential growth and saturation of near-equatorial MSWs occurred. Meanwhile, the dis-  
 593tribution functions at  $10$  and  $15^\circ$  latitudes exhibit the largest change between  $140 < t\Omega_{cp,eq} <$   
 594 $240$ , which corresponds to the growth and saturation of off-equatorial MSWs (aided by  
 595seed fluctuations from opposite hemispheres). Finally, at  $20^\circ$  latitude, this time is fur-  
 596ther delayed so that the largest change in the distribution function occurs between  $240 <$   
 597 $t\Omega_{cp,eq} < 320$ . On the other hand, since the wave intensity profile exhibits a sudden  
 598drop at around  $23^\circ$  latitude, the MSWs beyond this boundary are simply not strong enough  
 599to cause substantial scattering at  $25^\circ$  latitude. (The slight scattering there might have  
 600been caused by the numerical noise instead.)

601 In comparison with the local two-dimensional simulations of Min and Liu (2020)  
 602 (see also Figure S5), there is still plenty of free energy left at high latitudes, and in fact,  
 603 Figure 5b indicates trickling MSW excitation at later times. This is evidence that the  
 604 off-equatorial MSWs do not harness that free energy available efficiently because of the  
 605 strong equatorward refraction there and rapid detuning of resonance as waves propagate,  
 606 unless the backward seed fluctuations are sufficiently strong. (The low-resolution test  
 607 simulations indeed showed much faster evolution of the high-latitude distribution func-  
 608 tions (Boardsen et al., 2019).)

609 A comparison of Figures 11a and 11f clearly suggests that the energetic proton dis-  
 610 tribution at  $\lambda_{lat} = 25^\circ$ , which experienced little scattering, cannot simply be constructed  
 611 by projecting the equatorial distribution according to Liouville's theorem, which experi-  
 612 enced the most scattering. This indicates that the scattering of the energetic protons  
 613 and the evolution of their distribution functions are most likely local, despite an expect-  
 614 ation that mixing due to the field-aligned motion of particles would wash away any lo-  
 615 cal effect. The bounce period in a dipole field is given by  $\tau_b \approx (r_0/\sqrt{W_p/m_p})(3.7 -$   
 616 $1.6 \sin \alpha_{eq})$ , where  $W_p$  is the kinetic energy of the particle (Roederer, 1970). Plugging  
 617 in the representative parameters for the partial shell protons,  $r_0 = 770\lambda_{p,eq}$ ,  $W_p = m_p v_s^2/2$ ,  
 618 and  $\alpha_{eq} = 60^\circ$ , yields  $\tau_b \approx 1,480\Omega_{cp,eq}^{-1}$ . Since the total simulation duration (which is  
 619 about  $380\Omega_{cp,eq}^{-1}$ ) is roughly a quarter bounce period, the time scale of MSW excitation  
 620 (roughly  $80\Omega_{cp,eq}^{-1}$ ) is, in fact, shorter than the bounce period of the partial shell protons.

621 Figure 12 shows a comparison between the locally sampled partial shell proton dis-  
 622 tributions (black curve) and the distributions mapped from the instantaneous equatori-  
 623 al distributions following Liouville's theorem (red curve). The Liouville equilibria are  
 624 maintained initially up to  $t\Omega_{cp,eq} = 80$  for all latitudes, during which MSW activity is  
 625 low. Then, during the near-equatorial MSW saturation at  $t\Omega_{cp,eq} = 150$  the two types  
 626 of distributions exhibit the largest deviation, even at as low a latitude as  $\lambda_{lat} = 5^\circ$ , be-  
 627 cause the equatorial partial shell distribution is modified greatly as a result of the rapid  
 628 MSW excitation but the partial shell protons had no time to communicate the local ef-  
 629 fect to other latitudes. After that, the equilibrium is quickly restored at  $\lambda_{lat} = 5^\circ$ , and  
 630 mostly at  $\lambda_{lat} = 10^\circ$  by the end of the simulation. However, the distribution at  $\lambda_{lat} =$   
 631  $20^\circ$  still exhibits a large deviation (mostly at the low energy regime) at the end of the  
 632 simulation. Notably, the rate at which the equilibrium is restored is energy-dependent,  
 633 in accordance with the bounce period being energy-dependent.

634 Certainly, the re-distribution of the partial shell protons through the bounce mo-  
 635 tion should affect the subsequent development of MSWs at all latitudes. Unfortunately,

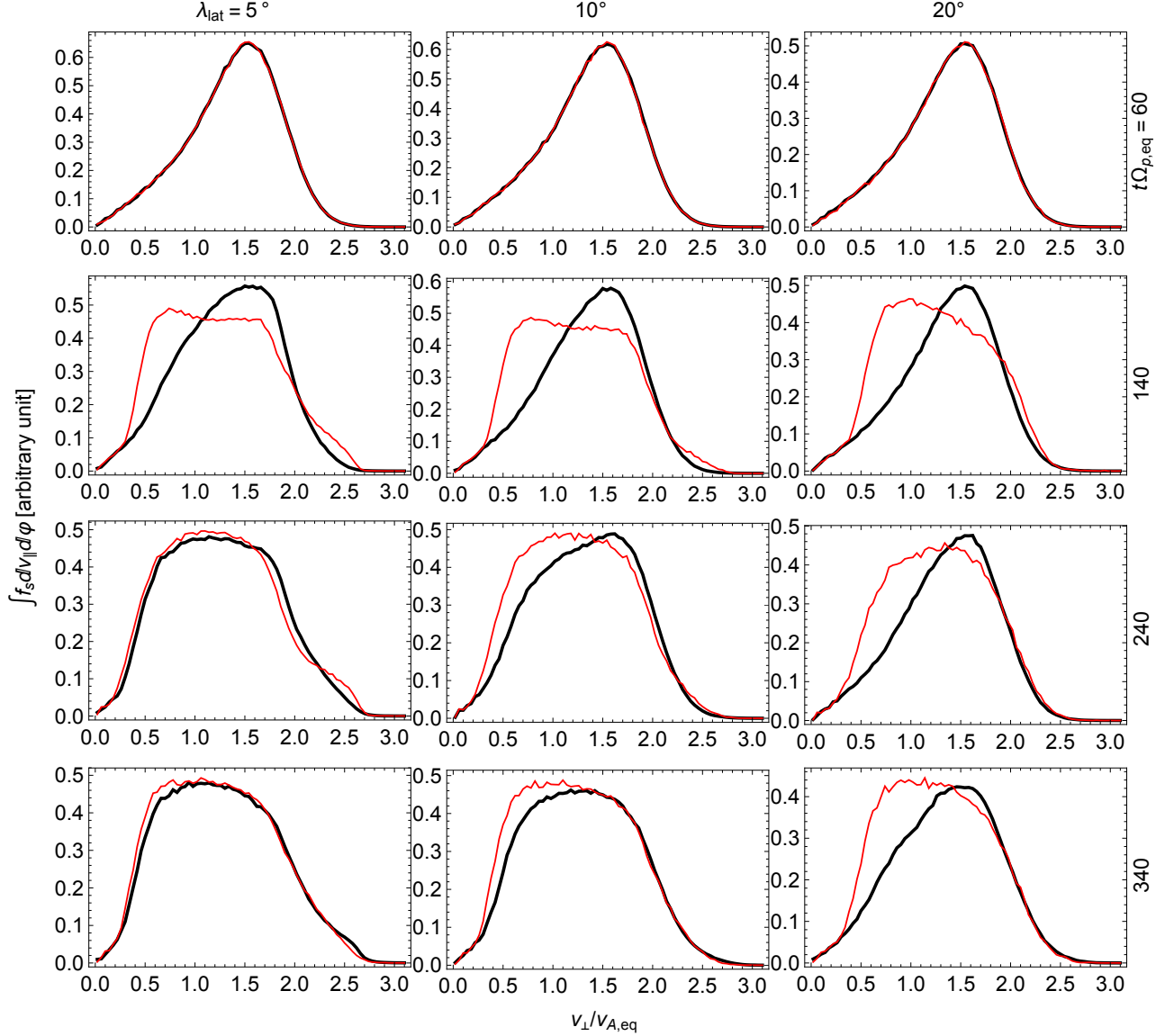


**Figure 12.** A comparison between the locally sampled partial shell proton distributions (black curve) and the distributions mapped from the instantaneous equatorial distributions following Liouville's theorem (red curve). The columns correspond to the selected latitudes (5, 10, and  $20^\circ$ ; top labels) and the rows correspond to the times of the distribution snapshots (60, 140, 240, and  $340\Omega_{cp,eq}^{-1}$ ; right labels).

636 the simulation run did not last long enough to assess this. Nevertheless, it is expected  
 637 that the subsequent wave growth will not be as explosive as the wave growth due to the  
 638 initial, pristine partial shell distributions, because the re-distribution time scale (that  
 639 is, the bounce time scale) is longer than the wave growth time scale. On the other hand,  
 640 based on the trend shown in Figure 12, we may project the subsequent development of  
 641 MSWs as follows. The protons strongly scattered toward lower energy at the equator  
 642 will move to high latitudes and reduce free energy by decreasing the positive slope of the  
 643 local partial shell distributions (see the last column of Figure 12), rendering further re-  
 644 duction of the wave growth there. Similarly, the protons relatively weakly scattered at  
 645 high latitudes will move to the equatorial region while yielding their free energy some-  
 646 where in between (depending on their local pitch angles and the local conditions).

## 647 5 Discussion

648 We stopped the simulation at  $t\Omega_{cp,eq} = 380$  for a few reasons. Practically, we al-  
 649 ready spent many cpu hours (equivalent to 30.6 days of wall clock time using 320 cpu  
 650 cores); and from the physics point of view, the system already passed the quasilinear sat-  
 651 uration phase and was nearing an equilibrium state. In addition, since our two-dimensional  
 652 simulation domain does not allow radial propagation of MSWs which tend to refract radially  
 653 outward in the dipole field (unless there exists a steep density gradient), we were  
 654 not tempted to continue the simulation and draw conclusions about the long-term be-  
 655 havior that might not be justified. On the other hand, under a suitable circumstance,  
 656 namely at the plasmopause (Kasahara et al., 1994; Chen & Thorne, 2012), MSWs can  
 657 indeed propagate in the azimuthal direction even beyond the source region with little  
 658 radial refraction. Motivated by this and also to understand the propagation outside the  
 659 source region, we removed all the energetic partial shell protons in the system and con-  
 660 tinued the simulation afterwards. Since these results are not essential for the conclusions  
 661 of the present study, we include the summary figures (similar to Figure 5) of this “long-  
 662 term” simulation in the supporting information and only state a few notable results here  
 663 (see Figures S6 and S7). Since there is no damping/growth, the MSWs thereafter con-  
 664 tinue propagating azimuthally while bouncing up and down latitudinally. The magnetic  
 665 field energy is contained well within  $\lambda_{lat} = \pm 10^\circ$ , whereas the electric field energy has  
 666 a non-negligible presence up to  $\lambda_{lat} = \pm 15^\circ$ , still consistent with the conclusion derived  
 667 earlier. Since the time scale for the continuous MSW excitation is shorter than the wave  
 668 packet bounce period (see Figures 5a and 5b), the wave packets are not uniform in time  
 669 and latitude, resulting in the bunching of wave packets and the modulation of amplitudes  
 670 in time and latitude. Contrary to the dominant equatorward Poynting flux during the  
 671 MSW growth phase, the Poynting flux outside the source region clearly exhibits a bi-  
 672 directional nature along the field line. Overall, it appears that we would have gotten the  
 673 same propagation pattern, had we traced a bundle of rays with the amplitudes prescribed  
 674 from the last point of the present simulation.

675 Since the present simulation is for one parameter set, it would be premature to gen-  
 676 eralize the present results for all possible combinations of key parameters. Nevertheless,  
 677 we make a few remarks on observation-simulation comparison. Recent statistical stud-  
 678 ies, particularly Boardsen et al. (2016) and Zou et al. (2019), have carried out compre-  
 679 hensive analyses of wave properties involving latitudinal dependence. It has been con-  
 680 sistent shown that MSWs are most frequently observed near the magnetic equator, which  
 681 any rightful model must demonstrate. Our simulation also showed a peak in intensity  
 682 centered at the magnetic equator, and this was achieved without localizing the free en-  
 683 ergy source to the magnetic equator. At the time of the primary wave saturation, the  
 684 difference in wave intensity at the equator and at  $\lambda_{lat} = 10^\circ$  was more than one order  
 685 of magnitude. At later times, however, the difference in magnitude was reduced, which  
 686 led to a broader peak of wave intensity versus latitude. Both Boardsen et al. (2016) and  
 687 Zou et al. (2019) have shown a similar trend, but the slope of wave intensity with respect

688 to latitude does not seem to agree: Zou et al. (2019, Figure 3) shows a much narrower  
 689 intensity peak with a steeper slope compared with Boardsen et al. (2016, Figures 10 and  
 690 11). Our result appears, at least for the present parameters, to be more consistent with  
 691 the result of Boardsen et al. (2016). We note that the present value for the equatorial  
 692 temperature anisotropy of energetic protons is small ( $A = 0.5$ ). The statistical study  
 693 by Thomsen et al. (2017) showed a wide range of  $A$  values, reaching as large a value as  
 694 10. So, since the source region can be further confined to the equatorial region for a larger  
 695 anisotropy of energetic protons (but not too large to excite EMIC waves), the use of a  
 696 value for  $A$  larger than assumed here can be one way to achieve the steeper gradient of  
 697 the MSW amplitudes shown by Zou et al. (2019).

698 On the other hand, the fact that the energetic partial shell protons do not neces-  
 699 sarily follow Liouville's theorem during MSW excitation begs a question of whether ini-  
 700 tializing the energetic protons according to Liouville's theorem in the simulation was re-  
 701 ally necessary. It could be that in reality the energetic ring-like protons (and hence the  
 702 source region) are indeed localized close to the magnetic equator by some physical mech-  
 703 anisms (such as injections), in which case Chen et al. (2018) may have been on the right  
 704 track. This suggests another way to achieve a steeper gradient of the MSW amplitudes,  
 705 where one takes a similar approach to Chen et al. (2018) but limiting the free energy source  
 706 near the magnetic equator without making the equatorial distribution unrealistically anisotropic.  
 707 Observationally, there may be two ways to judge which mechanism is more likely. First  
 708 is to explicitly measure whether there exists an extended ring-like feature during MSW  
 709 excitation using multi-spacecraft situated along the same field line; and second is to check  
 710 the direction of Poynting flux: A signature of converging Poynting flux may be indica-  
 711 tive of the extended source scenario.

712 Another recent notable result is the latitudinal dependence of the average wave nor-  
 713 mal angle produced by Zou et al. (2019). They reported that the median of wave nor-  
 714 mal angles maximizes at the equator and monotonically decreases with latitude (see Zou  
 715 et al., 2019, Figures 5 and 6). The median wave normal angle starts out from around  
 716  $88^\circ$  at the equator, falls monotonically with latitude, and reaches around  $85.5^\circ$  at  $15^\circ$   
 717 latitude. If this trend is a reasonable representation for the dominant wave modes, our  
 718 simulation seems to demonstrate a trend similar to their statistical study. Before hastily  
 719 jumping to the conclusion, however, we should note that Zou et al. (2019) made, as far  
 720 as their paper is concerned, no attempt to understand the impact of the larger error in  
 721  $\theta_{\mathbf{k}}$  associated with individual  $\theta_{\mathbf{k}}$  measurements and how it would impact their fitted curves.  
 722 Boardsen et al. (2016) estimated for the  $\theta_{\mathbf{k}}$  measurements greater than  $89.5^\circ$  the error  
 723 in  $\theta_{\mathbf{k}}$  to be  $2.54^\circ$  on average, based on eigenvalue analysis. Also, they showed using sim-  
 724 ulated data composed of multiple sine waves with randomly assigned  $\theta_{\mathbf{k}}$  between  $87$  and  
 725  $90^\circ$  that for the 55.6 Hz EMFISIS survey channel (Kletzing et al., 2013) the error in  $\theta_{\mathbf{k}}$   
 726 was  $5.6^\circ$  and that the spread in  $\theta_{\mathbf{k}}$  derived from polarization analysis of the simulated  
 727 data was similar to that of the observations (Boardsen et al., 2016, Figures 4 and 5). There-  
 728 fore, one does see a trend in  $\theta_{\mathbf{k}}$  with latitude in the EMFISIS survey data, but it seems  
 729 unclear as to what this trend means. Whether the observations corroborate our simu-  
 730 lation results or not, understanding how the MSW field structure varies with latitude  
 731 is important to quantitatively diagnose the resonant and non-resonant effect of MSWs  
 732 on energetic radiation belt electrons. So, a future study based on rigorous statistical anal-  
 733 ysis with more accurate  $\theta_{\mathbf{k}}$  measurements must be done to sort this out.

## 734 6 Conclusions

735 Here, two-dimensional PIC simulations were carried out with a simulation box on  
 736 a constant  $L$ -shell surface. Compared with the recent two-dimensional PIC simulation  
 737 study of MSWs in a meridional plane (Chen et al., 2018), the use of such an unconven-  
 738 tional simulation domain was motivated by the recent observational studies wherein prop-  
 739 agation of MSWs in the source region is dominantly in the azimuthal direction. Further-

740 more, we used a partial shell velocity distribution at the equator for energetic protons  
 741 which is only mildly anisotropic and therefore more realistic. This resulted in a wide lat-  
 742 itudinal extent of the free energy source following Liouville’s theorem. Overall, the present  
 743 simulation differed most significantly in these two aspects from the recent simulation study  
 744 in dipole geometry of Chen et al. (2018), and therefore, the results presented here can  
 745 be a good complement, or contrast, to theirs.

746 On the other hand, as in most PIC simulations, we had to use a reduced proton-  
 747 to-electron mass ratio and a smaller than realistic value for the light-to-Alfvén speed ra-  
 748 tio in order to reduce computation time. This altered the number of MSW harmonics  
 749 in the system and the time scale of MSW evolution. Nevertheless, the wave dispersion  
 750 relation was not greatly affected by the reduced ratios used and MSWs were driven by  
 751 the same physics. So, we can still get insight into the MSW generation process in the  
 752 presence of inhomogeneity along the field line, which is the primary goal of the present  
 753 study. Also, the hybrid approach was adopted where the dominant background proton  
 754 and electron populations were assumed to be cold. This helped lower the background  
 755 noise floor in the simulation. Finally, in a three-dimensional simulation domain the ra-  
 756 dial gradient of the dipole magnetic field and the plasma density would cause MSWs to  
 757 typically refract radially outward, while the present two-dimensional setup forced wave  
 758 packets to remain in one  $L$ -shell. This will not be a problem in the early stage of the sim-  
 759 ulation, but one may need to exercise caution when interpreting the present results at  
 760 later times.

761 The wave propagation and spectral characteristics presented here can be largely  
 762 understood from the purview of linear instability theory for local homogeneous plasmas  
 763 and the geometric optic framework for wave propagation in an inhomogeneous medium.  
 764 In fact, ray tracing is based upon these two principles. The main strength of the present  
 765 approach is that the wave and particle dynamics are self-consistently handled. Here are  
 766 some notable results.

- 767 1. Despite the extended unstable region in latitude owing to the use of a mild equa-  
 768 torial temperature anisotropy of the ring-like protons, MSWs excited at high lat-  
 769 itude are refracted equatorward and do not fully harness free energy available for  
 770 their amplification. This is consistent with the previous explanation (Boardsen  
 771 et al., 1992, 2016) that the equatorward refraction due to the field line gradient  
 772 of the dipole magnetic field prevents the high-latitude MSWs from staying in res-  
 773 onance (such that particle free energy is transferred to waves) with the energetic  
 774 protons for a sufficiently long time. On the other hand, the MSWs excited at the  
 775 equator experience much larger amplification, owing to the vanishing magnetic field  
 776 gradient there.
- 777 2. While exhausting free energy only slowly, the off-equatorial MSWs exhibit the sig-  
 778 natures of refraction and reflection suggested by the ray tracing analyses. In ad-  
 779 dition, the off-equatorial MSWs experience amplification at or near the reflection  
 780 points (where  $\theta_{\mathbf{k}}$  goes through  $90^\circ$ ) and are probably damped when crossing the  
 781 equator (where the wave normal direction is farthest from the perpendicular di-  
 782 rection). The Poynting flux is dominantly convergent toward the equator during  
 783 MSW growth and saturation, with occasional signatures of penetration across the  
 784 equator to the opposite hemispheres.
- 785 3. The MSWs in the present simulation exhibit a rather complex wave field struc-  
 786 ture varying with latitude. The simulated wave fronts are roughly aligned with  
 787 the dipole field in the vicinity of the equator (within  $\sim \pm 4^\circ$  latitude), and are slanted  
 788 somewhat away from that direction at higher latitude. Around  $15^\circ$  latitude the  
 789 power-weighted average wave normal angle is about  $85^\circ$ , and near the equatorial  
 790 region it is about  $87^\circ$  during the primary maximum of wave intensity; the latter  
 791 number varies depending on the relative strength between the waves originating  
 792 at the equator or off-equator.

- 793 4. In the equatorial region, the locally generated MSWs and the transient MSWs of  
 794 off-equatorial origin coexist. As a result, close to the equatorial region, the sim-  
 795 ulated frequency spectrograms exhibit both discrete spectral peaks at harmonics  
 796 of the local proton cyclotron frequency (to which the MSWs of the equatorial ori-  
 797 gin contribute) and a broad continuous spectrum extending beyond the lower hy-  
 798 brid frequency (to which the MSWs of the off-equatorial origin contribute). With  
 799 an increasing latitude, the discrete peaks weaken gradually and the continuous spec-  
 800 trum eventually dominates (at about  $15^\circ$ ), as a result of rapid detuning of reso-  
 801 nance as waves propagate and get refracted. In addition, the lower cutoff of the  
 802 unstable harmonics also shifts toward high harmonic number with an increasing  
 803 latitude so that the frequency-latitude spectrogram demonstrates the so-called funnel-  
 804 shaped structure.
- 805 5. Consistent with the quasilinear picture, energetic protons sampled at several lat-  
 806 itudes experience scattering in response to the MSW excitation in such a way as  
 807 to reduce the positive slope of the proton velocity distribution function in the per-  
 808 pendicular velocity direction. The degree to which the scattering occurs has a good  
 809 correlation with the instantaneous MSW intensity at a given latitude. Further-  
 810 more, the local energetic proton distributions do not follow Liouville's theorem on  
 811 the time scale of MSW excitation.

## 812 Acknowledgments

813 This work was supported by the National Research Foundation of Korea (NRF) grant  
 814 funded by the Korea government (MSIT) (No. 2020R1C1C1009996) and by research fund  
 815 of Chungnam National University. K.L.'s research is supported by National Natural Sci-  
 816 ence Foundation of China (NSFC) grant 41974168. Work at Dartmouth was supported  
 817 by NSF grant AGS-1602469 and also by NASA grant 80NSSC19K0270. F. Nemeč would  
 818 like to acknowledge the use of funds from GACR grant 18-00844S. At Goddard this study  
 819 was supported by NASA prime contract NAS5-01072. Y.M. is supported by JSPS Grant  
 820 (20H01959). This work was supported by the National Supercomputing Center with su-  
 821 percomputing resources including technical support (KSC-2019-CRE-0003). The numer-  
 822 ical simulations were also performed by using a high performance computing cluster at  
 823 the Korea Astronomy and Space Science Institute. Reduced datasets to produce the fig-  
 824 ures as well as the code used here are available in a Zenodo data repository at (doi: 10.5281/zen-  
 825 odo.3894005).

## 826 References

- 827 André, R., Lefeuvre, F., Simonet, F., & Inan, U. S. (2002, Jul). A first approach to  
 828 model the low-frequency wave activity in the plasmasphere. *Annales Geophysici-*  
 829 *caë*, *20*(7), 981-996. doi: 10.5194/angeo-20-981-2002
- 830 Boardsen, S. A., Gallagher, D. L., Gurnett, D. A., Peterson, W. K., & Green, J. L.  
 831 (1992, October). Funnel-shaped, low-frequency equatorial waves. *J. Geophys.*  
 832 *Res.*, *97*, 14. doi: 10.1029/92JA00827
- 833 Boardsen, S. A., Hospodarsky, G. B., Kletzing, C. A., Engebretson, M. J., Pfaff,  
 834 R. F., Wygant, J. R., . . . De Pascuale, S. (2016, April). Survey of the fre-  
 835 quency dependent latitudinal distribution of the fast magnetosonic wave mode  
 836 from Van Allen Probes Electric and Magnetic Field Instrument and Integrated  
 837 Science waveform receiver plasma wave analysis. *Journal of Geophysical Re-*  
 838 *search (Space Physics)*, *121*, 2902-2921. doi: 10.1002/2015JA021844
- 839 Boardsen, S. A., Hospodarsky, G. B., Min, K., Averkamp, T. F., Bounds, S. R.,  
 840 Kletzing, C. A., & Pfaff, R. F. (2018, August). Determining the Wave Vector  
 841 Direction of Equatorial Fast Magnetosonic Waves. *Geophys. Res. Lett.*, *45*,  
 842 7951-7959. doi: 10.1029/2018GL078695
- 843 Boardsen, S. A., Min, K., Liu, K., Denton, R. E., & Nemeč, F. (2019, December).

- 844 Particle-in-cell simulations of fast magnetosonic waves on a drift shell sur-  
 845 face in the dipole magnetic field. In *Agu fall meeting abstracts* (Vol. 2019,  
 846 p. SM51F-3251).
- 847 Bortnik, J., & Thorne, R. M. (2010, July). Transit time scattering of energetic elec-  
 848 trons due to equatorially confined magnetosonic waves. *Journal of Geophysical*  
 849 *Research (Space Physics)*, *115*, A07213. doi: 10.1029/2010JA015283
- 850 Chen, L. (2015, June). Wave normal angle and frequency characteristics of mag-  
 851 netosonic wave linear instability. *Geophys. Res. Lett.*, *42*, 4709-4715. doi: 10  
 852 .1002/2015GL064237
- 853 Chen, L., Maldonado, A., Bortnik, J., Thorne, R. M., Li, J., Dai, L., & Zhan, X.  
 854 (2015, August). Nonlinear bounce resonances between magnetosonic waves  
 855 and equatorially mirroring electrons. *Journal of Geophysical Research (Space*  
 856 *Physics)*, *120*, 6514-6527. doi: 10.1002/2015JA021174
- 857 Chen, L., Sun, J., Lu, Q., Wang, X., Gao, X., Wang, D., & Wang, S. (2018, Septem-  
 858 ber). Two-Dimensional Particle-in-Cell Simulation of Magnetosonic Wave Excita-  
 859 tion in a Dipole Magnetic Field. *Geophys. Res. Lett.*, *45*, 8712-8720. doi: 10  
 860 .1029/2018GL079067
- 861 Chen, L., & Thorne, R. M. (2012, July). Perpendicular propagation of magnetosonic  
 862 waves. *Geophys. Res. Lett.*, *39*, L14102. doi: 10.1029/2012GL052485
- 863 Chen, L., Thorne, R. M., Jordanova, V. K., & Horne, R. B. (2010, November).  
 864 Global simulation of magnetosonic wave instability in the storm time magne-  
 865 tosphere. *Journal of Geophysical Research (Space Physics)*, *115*, A11222. doi:  
 866 10.1029/2010JA015707
- 867 Denton, R. E. (2018, February). Electromagnetic Ion Cyclotron Wavefields in a Re-  
 868 alistic Dipole Field. *Journal of Geophysical Research (Space Physics)*, *123*(2),  
 869 1208-1223. doi: 10.1002/2017JA024886
- 870 Denton, R. E., Jordanova, V. K., & Fraser, B. J. (2014, Oct). Effect of spatial  
 871 density variation and O+ concentration on the growth and evolution of elec-  
 872 tromagnetic ion cyclotron waves. *Journal of Geophysical Research (Space*  
 873 *Physics)*, *119*(10), 8372-8395. doi: 10.1002/2014JA020384
- 874 Gulelmi, A. V., Klaine, B. I., & Potapov, A. S. (1975, February). Excitation of  
 875 magnetosonic waves with discrete spectrum in the equatorial vicinity of the  
 876 plasmopause. , *23*, 279-286. doi: 10.1016/0032-0633(75)90133-6
- 877 Gurnett, D. A. (1976, Jun). Plasma wave interactions with energetic ions near  
 878 the magnetic equator. *J. Geophys. Res.*, *81*(16), 2765. doi: 10.1029/  
 879 JA081i016p02765
- 880 Horne, R. B., & Miyoshi, Y. (2016, October). Propagation and linear mode conver-  
 881 sion of magnetosonic and electromagnetic ion cyclotron waves in the radiation  
 882 belts. *Geophys. Res. Lett.*, *43*(19), 10,034-10,039. doi: 10.1002/2016GL070216
- 883 Horne, R. B., Thorne, R. M., Glauert, S. A., Meredith, N. P., Pokhotelov, D., &  
 884 Santolík, O. (2007, September). Electron acceleration in the Van Allen radia-  
 885 tion belts by fast magnetosonic waves. *Geophys. Res. Lett.*, *34*, L17107. doi:  
 886 10.1029/2007GL030267
- 887 Horne, R. B., Wheeler, G. V., & Alleyne, H. S. C. K. (2000, December). Proton and  
 888 electron heating by radially propagating fast magnetosonic waves. *J. Geophys.*  
 889 *Res.*, *105*, 27597-27610. doi: 10.1029/2000JA000018
- 890 Hrbáčková, Z., Santolík, O., Němec, F., Macušová, E., & Cornilleau-Wehrin, N.  
 891 (2015, February). Systematic analysis of occurrence of equatorial noise emis-  
 892 sions using 10 years of data from the Cluster mission. *Journal of Geophysical*  
 893 *Research (Space Physics)*, *120*, 1007-1021. doi: 10.1002/2014JA020268
- 894 Hu, Y., & Denton, R. E. (2009, December). Two-dimensional hybrid code  
 895 simulation of electromagnetic ion cyclotron waves in a dipole magnetic  
 896 field. *Journal of Geophysical Research (Space Physics)*, *114*, A12217. doi:  
 897 10.1029/2009JA014570
- 898 Kasahara, Y., Kenmochi, H., & Kimura, I. (1994, July). Propagation characteris-

- tics of the ELF emissions observed by the satellite Akebono in the magnetic equatorial region. *Radio Science*, *29*, 751-767. doi: 10.1029/94RS00445
- 899  
900  
901 Katoh, Y., & Omura, Y. (2004, December). Acceleration of relativistic electrons  
902 due to resonant scattering by whistler mode waves generated by temperature  
903 anisotropy in the inner magnetosphere. *Journal of Geophysical Research (Space  
904 Physics)*, *109*(A12), A12214. doi: 10.1029/2004JA010654
- 905 Kletzing, C. A., Kurth, W. S., Acuna, M., MacDowall, R. J., Torbert, R. B.,  
906 Averkamp, T., ... Tyler, J. (2013, November). The Electric and Magnetic  
907 Field Instrument Suite and Integrated Science (EMFISIS) on RBSP. *Space  
908 Sci. Rev.*, *179*(1-4), 127-181. doi: 10.1007/s11214-013-9993-6
- 909 Laakso, H., Junginger, H., Schmidt, R., Roux, A., & de Villedary, C. (1990, July).  
910 Magnetosonic waves above fc(H+) at geostationary orbit - GEOS 2 results. *J.  
911 Geophys. Res.*, *95*, 10609-10621. doi: 10.1029/JA095iA07p10609
- 912 Li, X., & Tao, X. (2018, January). Validation and Analysis of Bounce Resonance  
913 Diffusion Coefficients. *Journal of Geophysical Research (Space Physics)*, *123*,  
914 104-113. doi: 10.1002/2017JA024506
- 915 Li, X., Tao, X., Lu, Q., & Dai, L. (2015, November). Bounce resonance diffusion co-  
916 efficients for spatially confined waves. *Geophys. Res. Lett.*, *42*, 9591-9599. doi:  
917 10.1002/2015GL066324
- 918 Liu, K., Gary, S. P., & Winske, D. (2011, July). Excitation of magnetosonic waves  
919 in the terrestrial magnetosphere: Particle-in-cell simulations. *Journal of Geo-  
920 physical Research (Space Physics)*, *116*, A07212. doi: 10.1029/2010JA016372
- 921 Lu, Q., Ke, Y., Wang, X., Liu, K., Gao, X., Chen, L., & Wang, S. (2019, Jun).  
922 Two-Dimensional gcPIC Simulation of Rising-Tone Chorus Waves in a Dipole  
923 Magnetic Field. *Journal of Geophysical Research (Space Physics)*, *124*(6),  
924 4157-4167. doi: 10.1029/2019JA026586
- 925 Ma, Q., Li, W., Bortnik, J., Kletzing, C. A., Kurth, W. S., Hospodarsky, G. B., &  
926 Wygant, J. R. (2019). Global Survey and Empirical Model of Fast Magne-  
927 tosonic Waves Over Their Full Frequency Range in Earth's Inner Magneto-  
928 sphere. *Journal of Geophysical Research (Space Physics)*, *124*(12), 10270-  
929 10282. Retrieved from [https://agupubs.onlinelibrary.wiley.com/doi/  
930 abs/10.1029/2019JA027407](https://agupubs.onlinelibrary.wiley.com/doi/abs/10.1029/2019JA027407) doi: 10.1029/2019JA027407
- 931 Ma, Q., Li, W., Thorne, R. M., & Angelopoulos, V. (2013, May). Global distribution  
932 of equatorial magnetosonic waves observed by THEMIS. *Geophys. Res. Lett.*,  
933 *40*, 1895-1901. doi: 10.1002/grl.50434
- 934 Meredith, N. P., Horne, R. B., & Anderson, R. R. (2008, June). Survey of mag-  
935 netosonic waves and proton ring distributions in the Earth's inner magneto-  
936 sphere. *Journal of Geophysical Research (Space Physics)*, *113*, A06213. doi:  
937 10.1029/2007JA012975
- 938 Min, K., Boardsen, S. A., Denton, R. E., & Liu, K. (2018, November). Equa-  
939 torial Evolution of the Fast Magnetosonic Mode in the Source Region:  
940 Observation-Simulation Comparison of the Preferential Propagation Direc-  
941 tion. *Journal of Geophysical Research (Space Physics)*, *123*, 9532-9544. doi:  
942 10.1029/2018JA026037
- 943 Min, K., & Liu, K. (2016, Jan). Proton velocity ring-driven instabilities in  
944 the inner magnetosphere: Linear theory and particle-in-cell simulations.  
945 *Journal of Geophysical Research (Space Physics)*, *121*(1), 475-491. doi:  
946 10.1002/2015JA022042
- 947 Min, K., & Liu, K. (2020, June). Linear Instability and Saturation Characteristics of  
948 Magnetosonic Waves along the Magnetic Field Line. *Journal of Astronomy and  
949 Space Sciences*, *37*, 85-94. doi: 10.5140/JASS.2020.37.2.85
- 950 Min, K., Liu, K., Denton, R. E., & Boardsen, S. A. (2018, September). Particle-in-  
951 Cell Simulations of the Fast Magnetosonic Mode in a Dipole Magnetic Field:  
952 1-D Along the Radial Direction. *Journal of Geophysical Research (Space  
953 Physics)*, *123*, 7424-7440. doi: 10.1029/2018JA025666

- 954 Min, K., Liu, K., & Gary, S. P. (2016, Mar). Scalings of Alfvén-cyclotron and ion  
 955 Bernstein instabilities on temperature anisotropy of a ring-like velocity distri-  
 956 bution in the inner magnetosphere. *Journal of Geophysical Research (Space*  
 957 *Physics)*, *121*(3), 2185-2193. doi: 10.1002/2015JA022134
- 958 Min, K., Liu, K., Wang, X., Chen, L., & Denton, R. E. (2018, January). Fast  
 959 Magnetosonic Waves Observed by Van Allen Probes: Testing Local Wave Ex-  
 960 citation Mechanism. *Journal of Geophysical Research (Space Physics)*, *123*,  
 961 497-512. doi: 10.1002/2017JA024867
- 962 Min, K., Němec, F., Liu, K., Denton, R. E., & Boardsen, S. A. (2019, Jun). Equa-  
 963 torial Propagation of the Magnetosonic Mode Across the Plasmopause: 2-D  
 964 PIC Simulations. *Journal of Geophysical Research (Space Physics)*, *124*(6),  
 965 4424-4444. doi: 10.1029/2019JA026567
- 966 Miyoshi, Y., Matsuda, S., Kurita, S., Nomura, K., Keika, K., Shoji, M., . . . Wygant,  
 967 J. F. (2019, June). EMIC Waves Converted From Equatorial Noise Due to  
 968  $M/Q = 2$  Ions in the Plasmasphere: Observations From Van Allen Probes and  
 969 Arase. *Geophys. Res. Lett.*, *46*(11), 5662-5669. doi: 10.1029/2019GL083024
- 970 Němec, F., Santolík, O., Gereová, K., Macúšová, E., de Conchy, Y., & Cornilleau-  
 971 Wehrlin, N. (2005, January). Initial results of a survey of equatorial noise  
 972 emissions observed by the Cluster spacecraft. *Planetary and Space Science*, *53*,  
 973 291-298. doi: 10.1016/j.pss.2004.09.055
- 974 Němec, F., Santolík, O., Hrbáčková, Z., & Cornilleau-Wehrlin, N. (2015, March). In-  
 975 tensities and spatiotemporal variability of equatorial noise emissions observed  
 976 by the Cluster spacecraft. *Journal of Geophysical Research (Space Physics)*,  
 977 *120*, 1620-1632. doi: 10.1002/2014JA020814
- 978 Němec, F., Santolík, O., Pickett, J. S., Hrbáčková, Z., & Cornilleau-Wehrlin, N.  
 979 (2013, November). Azimuthal directions of equatorial noise propagation deter-  
 980 mined using 10 years of data from the Cluster spacecraft. *Journal of Geophysi-  
 981 cal Research (Space Physics)*, *118*, 7160-7169. doi: 10.1002/2013JA019373
- 982 Němec, F., Santolík, O., Gereová, K., Macúšová, E., Laakso, H., de Conchy, Y., . . .  
 983 Cornilleau-Wehrlin, N. (2006, Jan). Equatorial noise: Statistical study of  
 984 its localization and the derived number density. *Advances in Space Research*,  
 985 *37*(3), 610-616. doi: 10.1016/j.asr.2005.03.025
- 986 Perraut, S., Roux, A., Robert, P., Gendrin, R., Sauvaud, J.-A., Bosqued, J.-  
 987 M., . . . Korth, A. (1982, August). A systematic study of ULF waves  
 988 above F/H plus/ from GEOS 1 and 2 measurements and their relation-  
 989 ships with proton ring distributions. *J. Geophys. Res.*, *87*, 6219-6236. doi:  
 990 10.1029/JA087iA08p06219
- 991 Posch, J. L., Engebretson, M. J., Olson, C. N., Thaller, S. A., Breneman, A. W.,  
 992 Wygant, J. R., . . . Reeves, G. D. (2015, August). Low-harmonic magnetosonic  
 993 waves observed by the Van Allen Probes. *Journal of Geophysical Research*  
 994 *(Space Physics)*, *120*, 6230-6257. doi: 10.1002/2015JA021179
- 995 Roberts, C. S., & Schulz, M. (1968, Dec). Bounce resonant scattering of particles  
 996 trapped in the Earth's magnetic field. *J. Geophys. Res.*, *73*(23), 7361-7376.  
 997 doi: 10.1029/JA073i023p07361
- 998 Roederer, J. G. (1970). *Dynamics of geomagnetically trapped radiation*. (Physics and  
 999 Chemistry in Space, Berlin: Springer, 1970)
- 1000 Russell, C. T., Holzer, R. E., & Smith, E. J. (1970). OGO 3 observations of ELF  
 1001 noise in the magnetosphere: 2. The nature of the equatorial noise. *J. Geophys.*  
 1002 *Res.*, *75*, 755. doi: 10.1029/JA075i004p00755
- 1003 Santolík, O., Němec, F., Gereová, K., Macúšová, E., Conchy, Y., & Cornilleau-  
 1004 Wehrlin, N. (2004, July). Systematic analysis of equatorial noise below  
 1005 the lower hybrid frequency. *Annales Geophysicae*, *22*, 2587-2595. doi:  
 1006 10.5194/angeo-22-2587-2004
- 1007 Santolík, O., Parrot, M., & Němec, F. (2016, July). Propagation of equatorial noise  
 1008 to low altitudes: Decoupling from the magnetosonic mode. *Geophys. Res. Lett.*,

- 1009 43, 6694-6704. doi: 10.1002/2016GL069582
- 1010 Santolik, O., Pickett, J. S., Gurnett, D. A., Maksimovic, M., & Cornilleau-Wehrin,  
1011 N. (2002, December). Spatiotemporal variability and propagation of equatorial  
1012 noise observed by Cluster. *Journal of Geophysical Research (Space Physics)*,  
1013 107, 1495. doi: 10.1029/2001JA009159
- 1014 Shklyar, D. R., & Balikhin, M. A. (2017, October). Whistler Mode Waves Be-  
1015 low Lower Hybrid Resonance Frequency: Generation and Spectral Fea-  
1016 tures. *Journal of Geophysical Research (Space Physics)*, 122, 10. doi:  
1017 10.1002/2017JA024416
- 1018 Shprits, Y. Y. (2009, June). Potential waves for pitch-angle scattering of near-  
1019 equatorially mirroring energetic electrons due to the violation of the sec-  
1020 ond adiabatic invariant. *Geophys. Res. Lett.*, 36, L12106. doi: 10.1029/  
1021 2009GL038322
- 1022 Sun, J., Gao, X., Lu, Q., Chen, L., Liu, X., Wang, X., . . . Wang, S. (2017, May).  
1023 Spectral properties and associated plasma energization by magnetosonic waves  
1024 in the Earth's magnetosphere: Particle-in-cell simulations. *Journal of Geophys-  
1025 ical Research (Space Physics)*, 122, 5377-5390. doi: 10.1002/2017JA024027
- 1026 Tao, X. (2014, May). A numerical study of chorus generation and the related varia-  
1027 tion of wave intensity using the DAWN code. *Journal of Geophysical Research  
1028 (Space Physics)*, 119, 3362-3372. doi: 10.1002/2014JA019820
- 1029 Tao, X., & Li, X. (2016, July). Theoretical bounce resonance diffusion coefficient for  
1030 waves generated near the equatorial plane. *Geophys. Res. Lett.*, 43, 7389-7397.  
1031 doi: 10.1002/2016GL070139
- 1032 Thomsen, M. F., Denton, M. H., Gary, S. P., Liu, K., & Min, K. (2017, Dec).  
1033 Ring/Shell Ion Distributions at Geosynchronous Orbit. *Journal of Geo-  
1034 physical Research (Space Physics)*, 122(12), 12,055-12,071. doi: 10.1002/  
1035 2017JA024612
- 1036 Umeda, T., Omura, Y., & Matsumoto, H. (2001, June). An improved mask-  
1037 ing method for absorbing boundaries in electromagnetic particle simula-  
1038 tions. *Computer Physics Communications*, 137, 286-299. doi: 10.1016/  
1039 S0010-4655(01)00182-5
- 1040 Walker, S. N., Balikhin, M. A., Shklyar, D. R., Yearby, K. H., Canu, P., Carr,  
1041 C. M., & Dandouras, I. (2015, Nov). Experimental determination of the  
1042 dispersion relation of magnetosonic waves. *Journal of Geophysical Research  
1043 (Space Physics)*, 120(11), 9632-9650. doi: 10.1002/2015JA021746
- 1044 Xiao, F., & Feng, X. (2006, May). Modeling Density and Anisotropy of Energetic  
1045 Electrons Along Magnetic Field Lines. *Plasma Science and Technology*, 8, 279-  
1046 284. doi: 10.1088/1009-0630/8/3/07
- 1047 Yuan, Z., Yao, F., Yu, X., Huang, S., & Ouyang, Z. (2019, May). An Automatic  
1048 Detection Algorithm Applied to Fast Magnetosonic Waves With Observations  
1049 of the Van Allen Probes. *Journal of Geophysical Research (Space Physics)*,  
1050 124(5), 3501-3511. doi: 10.1029/2018JA026387
- 1051 Zhima, Z., Chen, L., Fu, H., Cao, J., Horne, R. B., & Reeves, G. (2015, Novem-  
1052 ber). Observations of discrete magnetosonic waves off the magnetic equator.  
1053 *Geophys. Res. Lett.*, 42, 9694-9701. doi: 10.1002/2015GL066255
- 1054 Zou, Z., Zuo, P., Ni, B., Wei, F., Zhao, Z., Cao, X., . . . Gu, X. (2019, Jul). Wave  
1055 Normal Angle Distribution of Fast Magnetosonic Waves: A Survey of Van  
1056 Allen Probes EMFISIS Observations. *Journal of Geophysical Research (Space  
1057 Physics)*, 124(7), 5663-5674. doi: 10.1029/2019JA026556